Low-temperature cooling history of the Olympus-Ossa massif: new insights from zircon and apatite (U-Th)/He thermochronology and thermal modelling

Michael Walsh

Submitted in partial fulfillment of the requirements
for the Degree of Bachelor of Sciences, Honours

Department of Earth Sciences
Dalhousie University
Halifax, Nova Scotia
March 2013

Distribution License

DalSpace requires agreement to this non-exclusive distribution license before your item can appear on DalSpace.

NON-EXCLUSIVE DISTRIBUTION LICENSE

You (the author(s) or copyright owner) grant to Dalhousie University the non-exclusive right to reproduce and distribute your submission worldwide in any medium.

You agree that Dalhousie University may, without changing the content, reformat the submission for the purpose of preservation.

You also agree that Dalhousie University may keep more than one copy of this submission for purposes of security, back-up and preservation.

You agree that the submission is your original work, and that you have the right to grant the rights contained in this license. You also agree that your submission does not, to the best of your knowledge, infringe upon anyone's copyright.

If the submission contains material for which you do not hold copyright, you agree that you have obtained the unrestricted permission of the copyright owner to grant Dalhousie University the rights required by this license, and that such third-party owned material is clearly identified and acknowledged within the text or content of the submission.

If the submission is based upon work that has been sponsored or supported by an agency or organization other than Dalhousie University, you assert that you have fulfilled any right of review or other obligations required by such contract or agreement.

Dalhousie University will clearly identify your name(s) as the author(s) or owner(s) of the submission, and will not make any alteration to the content of the files that you have submitted.

If you have questions regarding this license please contact the repository manager at dalspace@dal.ca.

Grant the distribution license by signing and dating below.

_____   _____

Name of signatory   Date

DATE: April 28, 2013

AUTHOR: Michael Walsh

TITLE: Low-temperature cooling history of the Olympus-Ossa massif: new insights from zircon and apatite (U-Th)/He thermochronology and thermal modelling

Degree: B.Sc. (Hons)   Convocation: Fall   Year: 2013

Permission is herewith granted to Dalhousie University to circulate and to have copied for non-commercial purposes, at its discretion, the above title upon the request of individuals or institutions.

_____
Signature of Author

Acknowledgements

Abstract

The NW Aegean is a long-studied region experiencing Tertiary N-S extension in the rear of the South Hellenic Subduction Zone (Fig.1) (Gautier et al., 1999). There is some consensus that Aegean extension is the result of a southward migration of the Hellenic arc from rollback of the subducting slab (Berckhemer, 1977; e.g. Jolivet and Brun, 2010). The migration of this subduction zone creates a free boundary allowing the Aegean crust, previously thickened from Early Tertiary alpine collision, to gravitationally spread in a southward direction (e.g. Gauthier et al., 1999, Lacassin et al., 2007; Nance, 2010). Also impacting this region is the westward escape of Anatolia along the North Anatolian Fault (NAF) caused by the Middle to Upper Miocene collision of Arabia and Eurasia (e.g. Gautier et al., 1999, Lacassin et al., 2007) (Fig. 1). Recent studies suggest kinematic and mechanical interactions between Aegean extension and displacement along the right-lateral strike-slip North Anatolian Fault. The NAF propagated westward into the northern Aegean domain about 5 Ma ago, and is thought to have initiated a rapid phase of crustal cooling and exhumation at that time. (Lacassin et al., 2007, Flerit et al., 2004).

The Olympus-Ossa massif is located in the northwestern part of the Aegean domain, in the footwall of an active normal fault, and at the westward extent of the North Anatolian Fault and is an ideal site to test the influence of the NAF on Neogene crustal cooling (Fig. 1). The core of the modern Olympus-Ossa tectonic windows have been exhumed through divergent low-angle extensional shear zones (Killias et al., 2002) followed by high-angle normal faulting during the latest Tertiary-Quaternary (Schermer, 1993; Lacassin et al., 2007; Nance, 2010) at timing and rates that remain poorly constrained.

To test the hypothesis of the proposed post-5 Ma rapid cooling event, I investigated the Late Tertiary-Quaternary upper crustal cooling history of the Olympus-Ossa massif using apatite and zircon (U-Th)/He thermochronology on bedrock samples distributed in the tectonic windows and outside of them, across the Pelagonian domain. (U-Th)/He ages were combined with unpublished apatite fission-track data and used in the inverse thermal modelling software HeFTy (Ketcham, 2005) to provide constraints on the low-temperature cooling history of the region. The results show that a rapid cooling event occurred in the Olympus and Ossa massifs ~14-10 Ma ago, that lasted until ~9-5 Ma, suggesting that increased extension along the normal fault occurred prior to NAF propagation into the region, or that post-5 Ma cooling related to the NAF is not exposed in the modern landscape yet.

Table of Contents

Chapter 1 - Introduction

The Olympus-Ossa Massif contains the tallest peak in continental Greece (2,917 m), but the processes that led to its surface uplift and crustal cooling remain controversial (Lacassin et al., 2007; Gautier et al., 1999). It is located in the NW Aegean domain and at the western tip of the North Anatolian Fault (NAF) (Lacassin et al., 2007) (Fig.1). The NAF forms the boundary between the Aegean-Anatolian microplate and Eurasia, which were once a single cohesive unit until the propagation of the NAF separated them (Armijo et al., 1999). The Olympus-Ossa Massif basement belongs to the continental Hellenides, an orogen that was structured throughout the Early Tertiary during the convergence between the Eurasian and Apulian plates (Jolivet, 2010). It is comprised of metamorphosed and deformed Triassic and Cretaceous-Eocene limestones of the southwestern Neotethys Ocean, representing the passive margin of the Apulian Plate (Nance, 2010). During the Early Tertiary alpine collision, this passive margin was overridden by a series of thrust sheets including blueschist metamorphosed continental margin sediments, granitoid gneisses, schists, and ophiolites (Figs. 3, 6) (Nance, 2010). Following the collision, the Aegean domain was subjected to widespread post-orogenic extension starting ~26-40 Ma and ongoing today (Gautier et al., 1999). The Mesozoic limestones are now exposed within a tectonic window pierced through the overlying thrust nappes (Nance, 2010). The massif presumably underwent ~6-8 km of exhumation in response to processes and at times which remain a controversial subject (Nance, 2010).
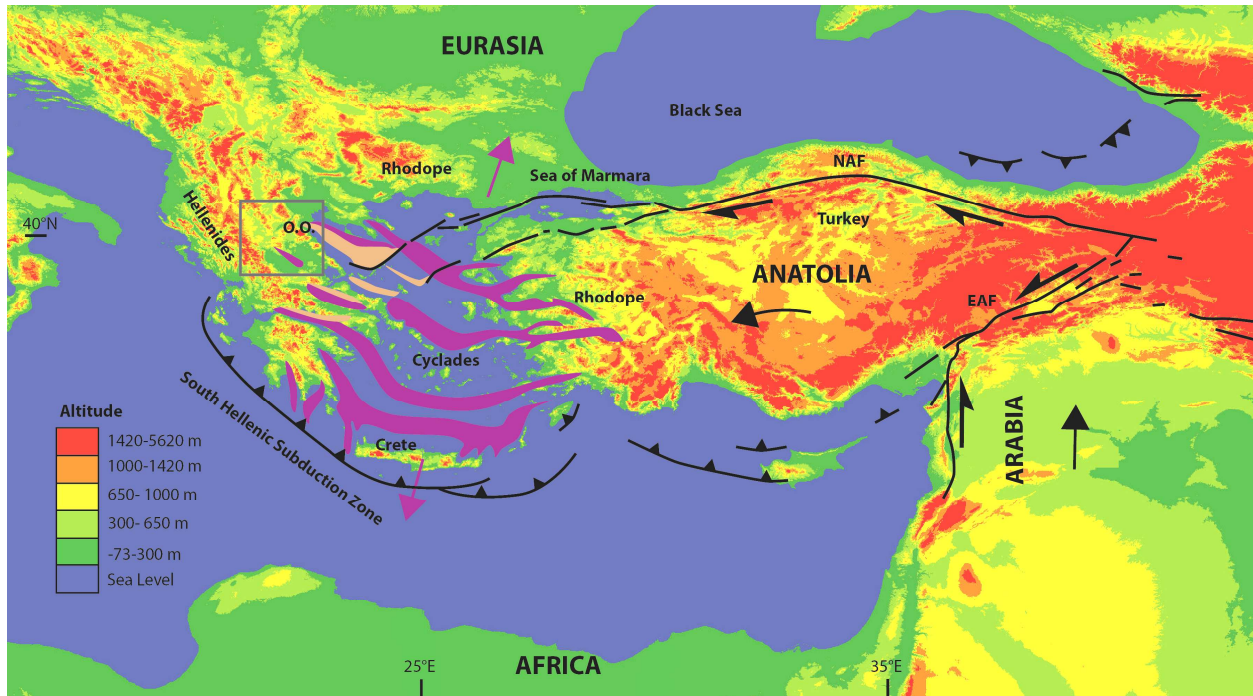
Figure 1: Geodynamic setting of the Aegean Domain. Violet arrows indicate overall direction of extension. Violet features indicate extensional domains that have been active within the last 15 years as documented by GPS data. Areas in beige have accelerated extension rates interpreted as being associated with the westward propagation of the NAF, grey square indicates the location of Figure 2 (study area). Abbreviations are: NAF = North Anatolian Fault; EAF = East Anatolian fault; O.O. = Olympus-Ossa massif. (Modified from Flerit et al., 2004)
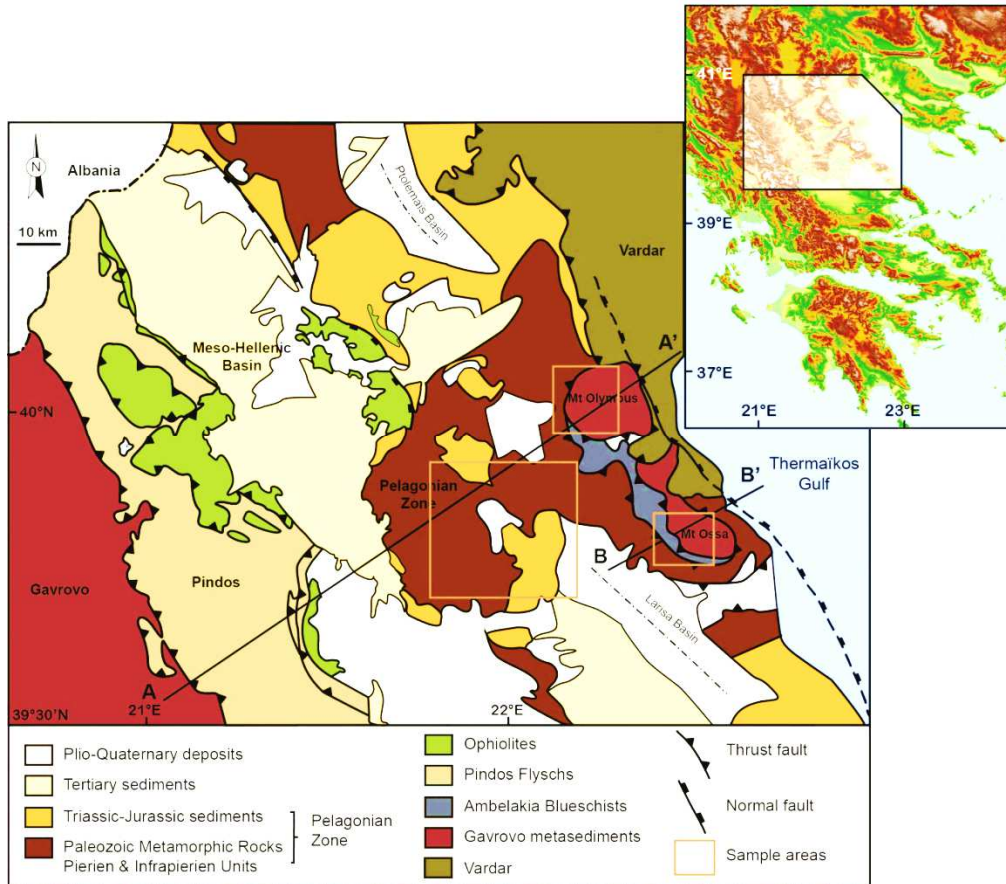
Figure 2: Geologic map showing main lithologic units in the Greek Hellenides (Modified from Ferrière et al., 2004), Samples were collected along A-A' and B-B' transects, within the three orange squares (see Fig. 3 & 17 for more details).
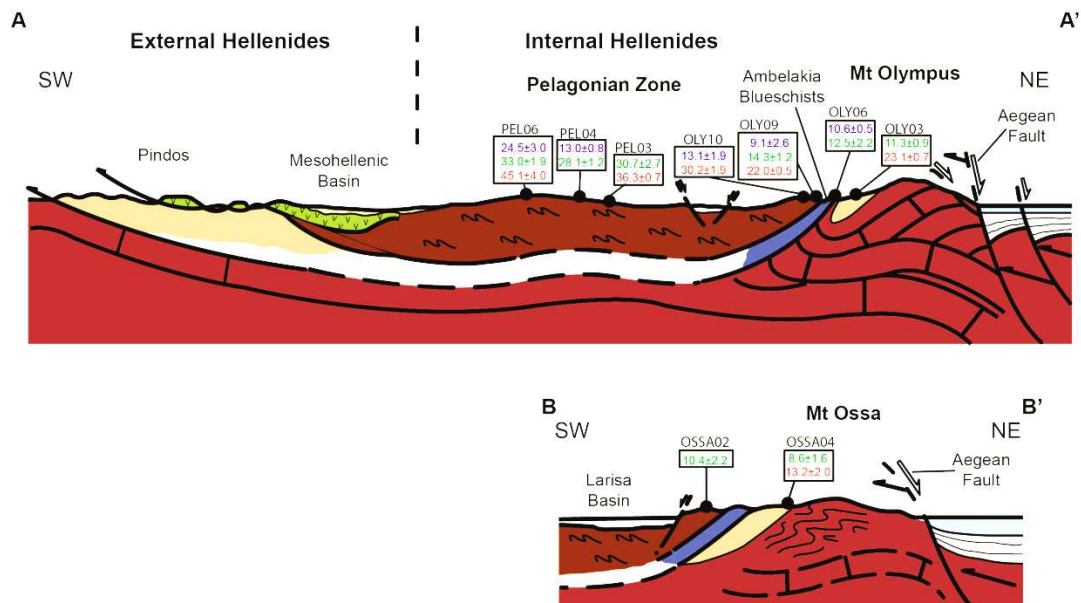
Figure 3 – Cross-sections of Mounts Olympus and Ossa along transects A-A' and B-B' located on Figure 2. Ages in blue and red are (U-Th)/He ages on apatite (AHe) and zircon (ZHe), respectively (this study), ages in green are unpublished apatite fission track ages (AFT). (Modified from Coutand et al., in prep.).

9

The uplift of the Olympus-Ossa Massif is interpreted as resulting from Early Neogene ductile shearing, and Neogene-recent brittle normal faulting along its eastern flank (Fig. 3). The limestones in the Mount Olympus tectonic window now form the uplifted and tilted footwall of northeastward dipping normal faults (Nance, 2010). Faulting and shearing deformation showing related direction of extension are seen throughout the Aegean domain (Gauthier et al., 1999, Lacassin et al., 2007). Aegean extension is widely thought to be the result of a southward migration of the Hellenic arc which lies to the south of the Aegean domain (Fig. 1) (Berckhemer, 1977; e.g. Jolivet and Brun, 2010). The migration of this subduction zone creates a free boundary allowing the Aegean crust, previously thickened and thermally weakened from the alpine collision, to gravitationally spread in a southward direction (e.g. Gauthier et al., 1999, Lacassin et al., 2007). Also impacting this region is the westward escape of Anatolia caused by the Middle to Upper Miocene collision of Arabia and Eurasia (Fig. 1)(Gautier et al., 1999). In the northern part of the system, recent studies suggest kinematic and mechanical interactions between the Aegean extension and displacement along the right-lateral strike-slip North Anatolian Fault, which propagated westward into the northern part of the Aegean around 5 Ma (Lacassin et al., 2007, Flerit et al., 2004).

The cooling and exhumation history of the Olympus-Ossa Massif in its various stages remains debated, although there is some consensus that both syn- and post-orogenic exhumation occurred (Lacassin et al., 2007; Jolivet and Brun, 2010). Previous studies have proposed that exhumation is the result of three rapid phases (the timing of which depend largely on timing estimates of specific causal processes) (Lacassin et al., 2007): the first and main episode is thought to have occurred at about 40 Ma and was coeval with nappe stacking due to contractional deformation; the second phase of exhumation occurred ~15-28 Ma ago, coeval to Aegean back-arc extension; the third and final phase of exhumation occurred ~ 5 Ma ago, and is coeval to the westward propagation of the NAF into the Aegean domain.

The Olympus-Ossa Massif is a crucial study area for Aegean extension because: it is located in the footwall of a major active normal fault with an accelerated extension rate thought to be associated with the westward propagation of the NAF into the region, and it is near the western extremity of the NAF (Flerit et al., 2004). It is therefore relevant in determining temporal relationships between cooling, Aegean back-arc extension, and NAF propagation (Lacassin et al., 2007). The purpose of this thesis is to constrain the Late Tertiary-Quaternary upper crustal cooling history of the Olympus-Ossa massif, and test the hypothesis of the proposed rapid

phase of cooling around 5 Ma. To this end, we process apatite and zircon (U-Th)/He thermochronology on bedrock samples collected across the Pelagonian domain in Northern Greece. (U-Th)/He thermochronology involves measurement of uranium, thorium, and helium to provide single-grain cooling ages at which apatite and zircon crystals cooled below closure temperatures of 70°C and 180°C, respectively (Farley, 2002). (U-Th)/He ages will be coupled with unpublished apatite fission-track data and used in the inverse thermal modelling software HeFTy (Ketcham, 2005) to provide a low-temperature cooling history for the region.

Chapter 2 - Geologic Setting

2.1 Geodynamic setting of the Aegean Domain

2.1.1. Alpine Collision, and syn-orogenic events

The Apulian plate collided with the Eurasian plate during the early Tertiary to form the Hellenic Alps (Schermer, 1990; Nance, 2010). Olympus and Ossa massifs are tectonic windows, composed of carbonate rocks of the external (western) Hellenides exposed through overlying metamorphic rocks of the internal (eastern) Hellenides (Figs. 2 & 3) (Schermer, 1990; Nance, 2010). Details regarding the number, age and magnitude of deformational phases related to this orogeny remain controversial due to the complex geologic history of the internal Hellenides (Schermer, 1990).

Continental Apulia underwent more than 400 km of shortening as it moved towards thenortheast, which led to the northeastward subduction of its passive margin leading edge, known as the Gavrovo-Tripolitsa unit, underneath the Pelagonian Zone. (Figs. 4b & c) (Schermer, 1990; Nance, 2010).

The Pelagonian zone, representing Paleozoic to Mesozoic metamorphic rocks of the internal Hellenides, was a microcontinental fragment separated from the Apulian Plate to the west by the Pindos Ocean, and from Rhodope to the east by the Vardar Ocean (Figs. 2 & 4a) (Schermer, 1990; Ferriere et al., 2004). In the internal Hellenides, obduction of Middle Jurassic ophiolites of the Vardar Ocean mark the onset of contractional deformation, which continued during the Cretaceous and Tertiary, progressing from east to west into the external Hellenides, emplacing obducted ophiolites atop the Pelagonian Zone (Fig. 4a) (Schermer, 1990; Ferriere et al., 2004). The Meso-Hellenic Basin, which now contains as much as 5 km of Cenozoic sediment, underwent subsidence during the Oligocene and Miocene, originating as a forearc basin during the subduction of the Pindos ocean (Figs. 4c & d) (Schermer, 1990; Ferriere et al., 2004; Jolivet and Brun, 2010). The Vardar zone east of the Olympus-Ossa massif, consisting

primarily of ophiolites extending northward to the Dinarides in Macedonia is thought to be the suture zone of the Pelagonian to the west and Rhodope to the east (Figs. 2, 4a) (Schermer, 1990; Nance, 2010). Ophiolites in the internal Hellenides represent the obducted Vardar ocean (Fig. 4a) (Ferriere et al., 2004), although some authors suggest it may also originate from the subducted remains of the Pindos ocean (Figs. 2 & 4) (see details of controversy in Schermer, 1990; Ferriere et al., 2004).

Lithotectonic units of the Olympos-Ossa massif are the result of nappe stacking during the collision and can be divided into four units (to be discussed in more detail in section 2.2.1). Listed from top to bottom these are (1) dismembered ophiolites; (2) Paleozoic continental basement rocks of the Pelagonian zone divided into the Pierien and Infrapierien units; (3) Ambelakia unit; (4) Olympos-Ossa unit (Figs. 2 & 6) (Schermer, 1990; Nance, 2010; Ferriere et al., 2004). Stratigraphic data to the north and south of Mt Olympus constrain the timing of ophiolite emplacement between late Jurassic and pre-Cenomanian (Schermer, 1990). Phengite mica $^{40}Ar/^{39}Ar$ ages constrain the timing of Infrapierien greenschist facies or blueschist-greenschist transition facies metamorphism to 100 Ma (Schermer, 1990). Rb/Sr and $^{40}Ar/^{39}Ar$ data retrieved from most of the blueschist-grade samples from Ambelakia and Pierien units indicate that blueschist mineral formation, foliation formation and isoclinal folding occurred between 53-61 Ma and is thought to coincide with the closure of the Neotethys Ocean (Vardar) (Schermer, 1990). Between 36-40 Ma, thrusting of blueschists of the Ambelakia and Pierien units over Olympos-Ossa units is interpreted from $^{40}Ar/^{39}Ar$ spectra from hornblende, biotite and white mica, and mylonites from these thrust faults show textural and mineralogical evidence suggesting high pressure, low temperature metamorphism (Schermer, 1990; Nance, 2010). Thrusting was directed in a south-west direction, placing higher pressure rocks from the internal Hellenides on top of lower pressure rocks from the external Hellenides (Figs. 3, 6) (Schermer, 1990). The underthrusted Gavrovo unit may be experiencing duplexing, creating localized uplift near the normal fault (Fig. 4f) (Ferriere et al., 2004). Lacassin et al. (2007) suggested from

structural observations and $^{40}Ar/^{39}Ar$ dating on white micas that normal ductile detachment was occurring contemporaneously with final nappe stacking between 43-49 Ma and caused a rapid phase of exhumation. These normal detachment faults are not proposed to be tectonically related to Aegean back-arc extension which is thought to have occurred in the Oligocene (Lacassin et al., 2007). An alternate theory was proposed by Jolivet and Brun (2010), that syn-orogenic exhumation occurred due to slab rollback during the subduction of the Pindos ocean during the upper Eocene, causing an early extensional episode which was interrupted by the arrival of the Apulian plate within the subduction zone in the early Oligocene.
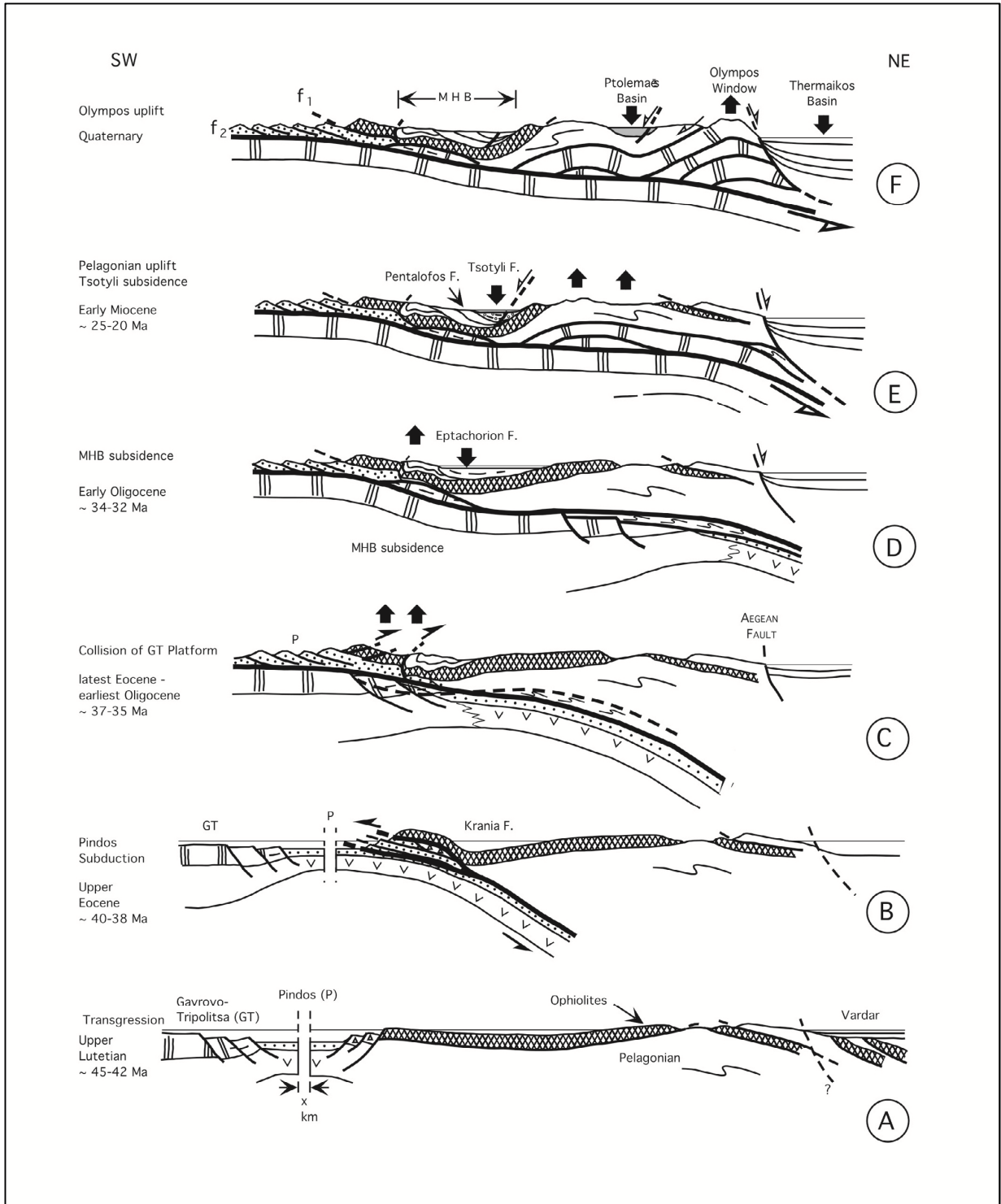
Figure 4: Tertiary geodynamic and tectonic evolution model of the NW Aegean, from the Gavrovo-Tripolitsa platform in the East to the Vardar ocean in the west. For location and orientation, see Figure 2. Abbreviations: MHB = Meso-Hellenic Basin (From Ferriere et al., 2004).

2.1.2. Hellenic arc migration and back-arc extension

The southward migration of the South Hellenic Subduction Zone (SHSZ), in combination with gravitational spreading of a thickened Aegean lithosphere are thought to be the main driving factors triggering Aegean extension (Fig. 1) (Gautier et al., 1999; Lacassin et al., 2007; Jolivet and Brun, 2010). At the SHSZ, northward subduction of the dense African plate generates slab pull forces as it sinks into the asthenospheric mantle of the overriding plate, underneath the Aegean Sea; this induces rollback of the African slab which retreats southwards (Gautier et al., 1999; Jolivet and Brun, 2010). Another gravitational force acting in the Aegean domain is the margin push force, originating from the lateral gradient in lithostatic pressure generated by the difference in elevation between the continental and oceanic lithospheres at the subduction zone (Gautier et al., 1999).

A large number of studies throughout the Aegean domain, particularly of the metamorphic core complexes of Cenozoic age, have been undertaken to constrain the space-time distribution of Aegean extension (e.g. Gautier et al., 1999). In the Olympos-Ossa massif, this extension has led to at least two generations of normal faults cutting through the overlying nappes (Schermer, 1990). In the Pierien unit, $^{40}Ar/^{39}Ar$ data on microcline constrain the age of deformation associated with normal faulting to 16-23 Ma (Schermer, 1990). In the Cyclades, radiometric and stratigraphic data indicate 21 Ma as the minimum age for the onset of extension seen in several north dipping extensional detachment zones (e.g. Gautier et al., 1999). Near the Rhodope massif, the Symvolon-Kavala granodiorite intruded contemporaneously with a sub-horizontal shear zone associated with Aegean extension and its age constrained by $^{206}Pb/^{238}U$ on titanite at 21-19 Ma, and $^{40}Ar/^{39}Ar$ ages on hornblende at 22-20 Ma (e.g. Gautier et al., 1999). On the nearby island of Thassos, ductile deformation of a major extensional decollement is constrained by Rb-Sr ages on white mica at 24-18 Ma, and $^{206}Pb/^{238}U$ ages at 22-20 Ma (Gautier et al., 1999). There are two principal grabens cutting across the Menderes massif trending east-west, of which evidence suggests that the sedimentary fill was deposited from original north-south directed extension (Gautier et al., 1999). Radiometric dating in these sediments constrains the

age to 20-14 Ma, and K-Ar data on biotite in a tuffite layer in one graben are dated at 21 Ma (Gautier et al., 1999). In Crete, fission track ages on zircon suggest that the onset of detachment-type extension occurred around 19 Ma (Thompson et al., 1998). These studies suggest that Aegean extension was already active across the Aegean domain by at least ~21 Ma (Gautier et al., 1999).

Lower Miocene extensional strain is documented by retrogressive mineral assemblages in the Cenozoic metamorphic core complexes (Gautier et al., 1999). The distribution and paleo-direction of stretching direction of Lower-Miocene extension are similar to those described for Pliocene-Lower Pleistocene, and also indicate a post orogenic origin (Gautier et al., 1999). This extension is sub-parallel with the convergence direction of the African plate and Aegean domain, whereas a syn-collisional extension would likely be directed east-west towards less-constrained boundaries (Gautier et al., 1999).

Extension according to this model is proposed to have started at initiation of subduction at the former South Hellenic passive margin (Gautier et al., 1999). Gravitational spreading of the already thickened Aegean lithosphere is directed to the less constrained free boundary of the SHSZ, so it is important to consider the timing of onset of subduction (Gautier et al., 1999). Seismic tomography analysis of the SHSZ reveals that the northward subducting African slab extends to a depth of at least 600 km, and a minimum age of onset of subduction estimated at 26-40 Ma (Gautier et al., 1999). This suggests that by the Lower Miocene, subduction was already active south of the Aegean domain (Gautier et al., 1999).

2.1.3. North Anatolian Fault (NAF) and extrusion of Anatolia

Many studies have suggested that initiation of Aegean extension resulted from the westward escape of Anatolia away from the Arabia-Eurasia collision front (Fig. 1), but temporal

discrepancies suggest this might not be likely (Gautier et al., 1999). Anatolia escapes along the NAF towards the free boundary of the SHSZ (Fig 1) (Gautier et al., 1999). Because the Aegean is bounded to the west by the Apulian plate, the Aegean deforms internally resulting in tension-gash type N-S extension (Figure 1) (Gautier et al., 1999). The NAF shows a present-day slip rate tapering towards its western end which appears to be associated with damaged Aegean lithosphere from previous stretching (Flerit et al., 2004).

The NAF enters the Aegean domain near the Dardanelles and the Sea of Marmara (Fig. 1) (Armijo et al., 1999). In the Dardanelles, folded structures associated with the propagating NAF were eroded and overlain by transgressive marine sediments of Messinian-early Pliocene age ~5 Ma (Ryan and Cita, 1978; Armijo et al., 1999). Once the tip of the NAF first reached the Aegean domain, Aegean back-arc extension began to control the velocity at which slip occurred (Flerit et al., 2004). It is suggested that the extrusion of Anatolia is now mechanically influenced by subduction zone dynamics in the SHSZ, and that events in the subduction zone should correlate with events throughout the NAF to the northeast (Flerit et al., 2004).

Low Middle Miocene Marine sedimentation rates in the suture zone of Arabia and Eurasia indicate a small difference in elevation between the collision zone and surrounding regions (Gautier et al., 1999). This unthickened lithosphere would not have induced any extrusion of Anatolia before the Middle Miocene, around 16 Ma (Gautier et al., 1999). Westward displacement of Anatolia is accommodated by the NAF, and right-lateral strike-slip displacement along this fault is thought to have initiated around 16 Ma as well, as evidenced by Middle Miocene sedimentation in elongated basins near the eastern extent of the NAF (Gautier et al., 1999).

As clockwise rotation of normal faults progressed in the NW Aegean (see section 2.2.2), extension direction is thought to have rotated to remain perpendicular to normal faulting (Fig. 8) (Gautier et al., 1999). Moment tensor solutions of regional normal faulting earthquakes and newly formed E-W striking onshore and offshore active normal faults south of the Olympos and Ossa massifs in Pelion indicate a return to more N-S extension and is interpreted as marking the onset of NAF induced deformation in the NW Aegean (Gautier et al., 1999; Lacassin et al., 2007). Near Pelion, south of the Olympus-Ossa massif, Lacassin et al. (2007) produced ^{40}Ar/^{39}Ar dates of 5.3 Ma and 3.9 Ma on K-Feldspar from a dyke which has been cut by more recent joints striking N80 to N110^{o}E suggesting presumably that NAF associated deformation was occurring in the NW Aegean after ~4 ma (Fig. 5).
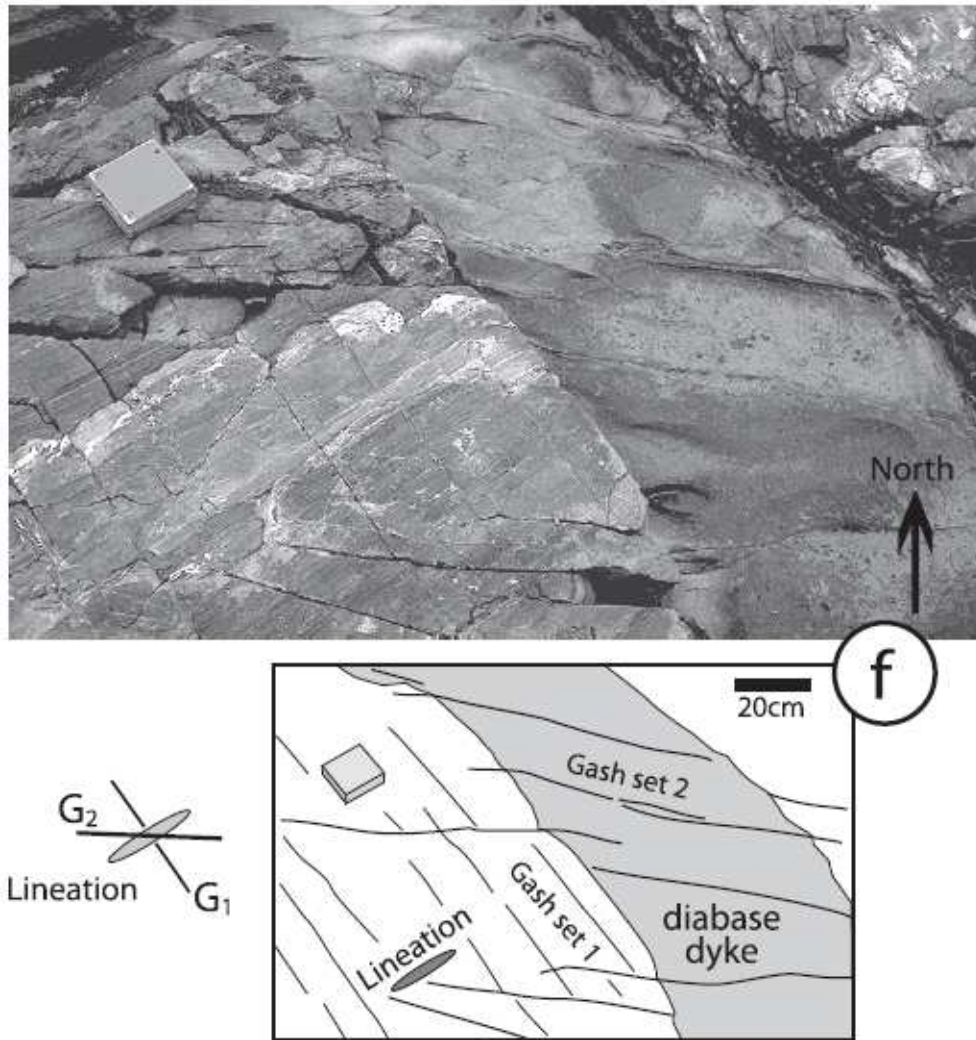
Figure 5: Deformation characteristics along the Aegean coast near Pelion. Lineation direction, gash set 1, and later dyke emplacement associated with sense of ductile deformation which has undergone rotation. Gash set 2 are more recent joints associated with NAF induced deformation in the NW Aegean (From Lacassin et al., 2007).

Although the NAF propagation into the Aegean domain seems well constrained at ~5 Ma, some evidence exists that structural discontinuities were in existence to the west of its leading tip. The strike-slip Ganos fault is a segment of the NAF separating the Dardanelles from a section of European Turkey (Fig. 1) (Hejl et al., 2010). Yaltirak and Alpar (2002) conducted structural investigations of the Ganos fault which indicate activation of the fault in the early Miocene, before being incorporated into the westward propagating NAF. Apatite fission-track (AFT) data from the island of Samothrake, in the shoulder of an active pull-apart basin situated

north of the NAF, suggest fast cooling as a result of transtension occurring between 14-10 Ma (Hejl et al., 2010).

2.2 Geology and structure of the Olympus-Ossa Massif

2.2.1. Lithology

The area surrounding Mount Olympus has been divided into four principal tectonostratigraphic thrust units (fig. 6), listed top to bottom these are: (1) dismembered Jurassic ophiolites; (2) Paleozoic continental basement rocks of the Pelagonian zone further divided into the Pierien and Infrapierien units, imbricated so that Infrapierien rocks are found both above and below Pierien rocks; (3) continental margin Ambelakia unit; and the (4) para-autochthonous Triassic to Eocene Olympos-Ossa unit (Fig. 2) (Schermer, 1990; Ferriere, 2004; Nance, 2010). The Paleozoic granitic basement of the Pierian unit was emplaced ~302 Ma ago, was exposed at surface and overlain by metasedimentary Permo-Triassic rocks, and subsequent Triassic-Jurassic marbles (Schermer, 1990; Nance, 2010). It consists primarily of granite and granitic gneisses with a thick marble cover, and contains zones of varying degrees of mylonitization (Schermer, 1990; Nance, 2010). High pressure conditions are indicated from a high phengite content of the micas (Schermer, 1990). The infrapierien unit consists of quartzofeldspatic and amphibolitic gneiss, mica schist, minor granite, with a thin marble cover, with evidence of at least three periods of deformation and metamorphism (Schermer, 1990). The Ambelakia unit consists of continental margin carbonates, quartzofeldspathic sedimentary rocks, and mafic to intermediate volcanic rocks metamorphosed at high grade (blueshist facies) (Schermer, 1990; Nance, 2010). The Olympos-Ossa unit is the subducted and exhumed tectonic window of the Gavrovo-Tripolitsa unit, and consists of a series of Triassic pelitic sediments and volcanics,

overlain by Late Triassic to Eocene carbonate platform sequence and Eocene flyschs (Fig. 2 & 3) (Schermer, 1990; Nance, 2010; Jolivet and Brun, 2010).
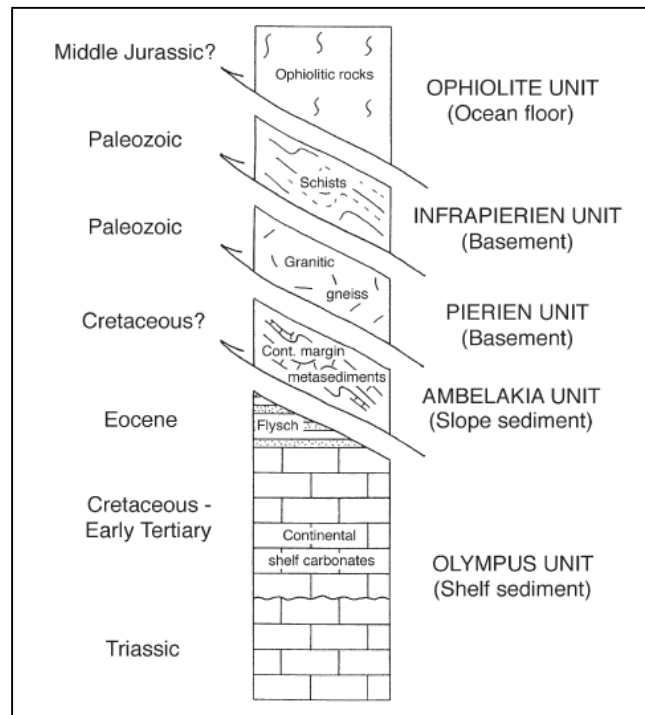
Figure 6 – Thrust sheets of the Olympus-Ossa Massif (From Nance, 2010, after Shermer et al., 1990)

2.2.2 Description of faults and deformation

The Olympos-Ossa massif is the uplifted footwall of the north-east dipping normal Aegean fault located off its eastern flank, with an average strike of N160°E (Fig. 7) (Lacassin et al., 2007). Further offshore in the North Aegean trough, N90° to N120°E striking normal faults are connected to strike-slip fault segments related to the northern branch of the NAF (Lacassin et al., 2007). The eastern piedmont of Mt Olympos is marked by several fault scarps striking N110° to N130°E which cut the normal Aegean fault obliquely, and are a prolongation of the offshore normal faults (Lacassin et al., 2007; Nance, 2010). Triangular facets are visible along the Aegean fault, indicating a steep dip, which are sub parallel to foliation in the metamorphic core (Lacassin et al., 2007). This foliation exibits stretching lineations in a N55°E direction, dips 20° to 30°E, and suggests that normal faulting has exhumed an earlier ductile deformation, transverse to the modern strike of the Aegean fault (Lacassin et al., 2007). Paleomagnetic data on

Neogene rocks were collected throughout the western Aegean, and suggest that domains which exhibit a present day NE-SW stretching direction have undergone clockwise rotation, whereas domains with a present day N-S stretching direction have not undergone rotation (Fig. 8) (Gautier et al., 1999; Jolivet and Brun, 2010). In the eastern Aegean and Cyclades, counterclockwise rotation has been documented but the overall pattern is more complicated (Fig. 8) (Gautier et al., 1999; Jolivet and Brun, 2010). The pattern of these rotations (Fig. 8) can be explained by a linear feature fixed at two ends and stretched laterally into a semi-circle. As the centre displaces further, the amount of rotation increases towards the fixed ends which have a greater curvature. This data suggests a Lower Miocene horst and graben system trending WNW-ESE which was subsequently and preferentially rotated as extension progressed (Gautier et al., 1999). The Olympos-Ossa massif has undergone approximately 28°-50° of clockwise rotation since ~15 Ma (Gautier et al., 1999; Lacassin et al., 2007; Jolivet and Brun).
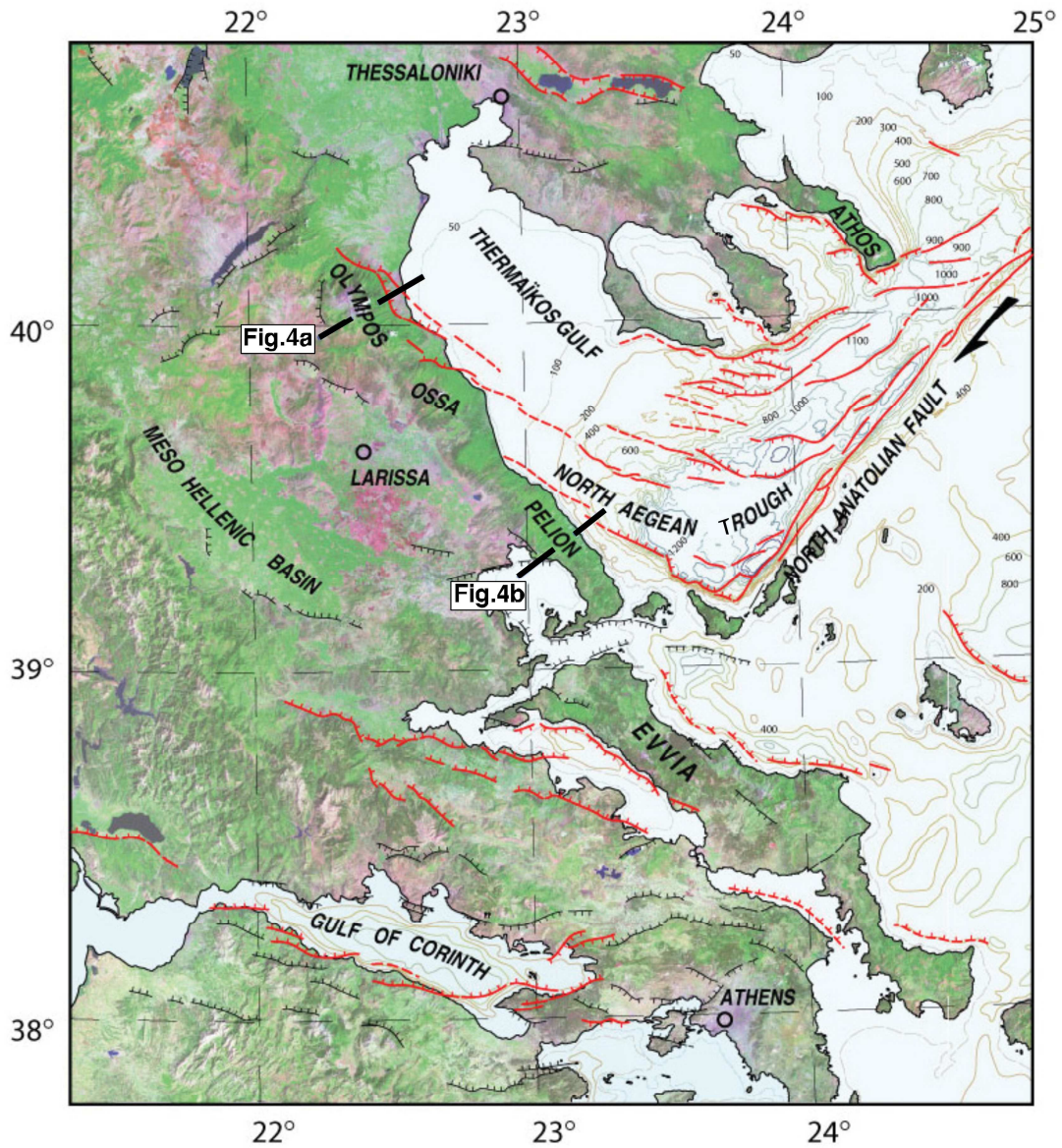
Figure 7: Map of recent faults in the Aegean NW Aegean. Major active faults are shown in red: NE-SW strike-slip faults associated with the North Anatolian Fault; NW-SE and E-W are extensional normal faults. Secondary faults are noted in black (From Lacassin et al., 2007).
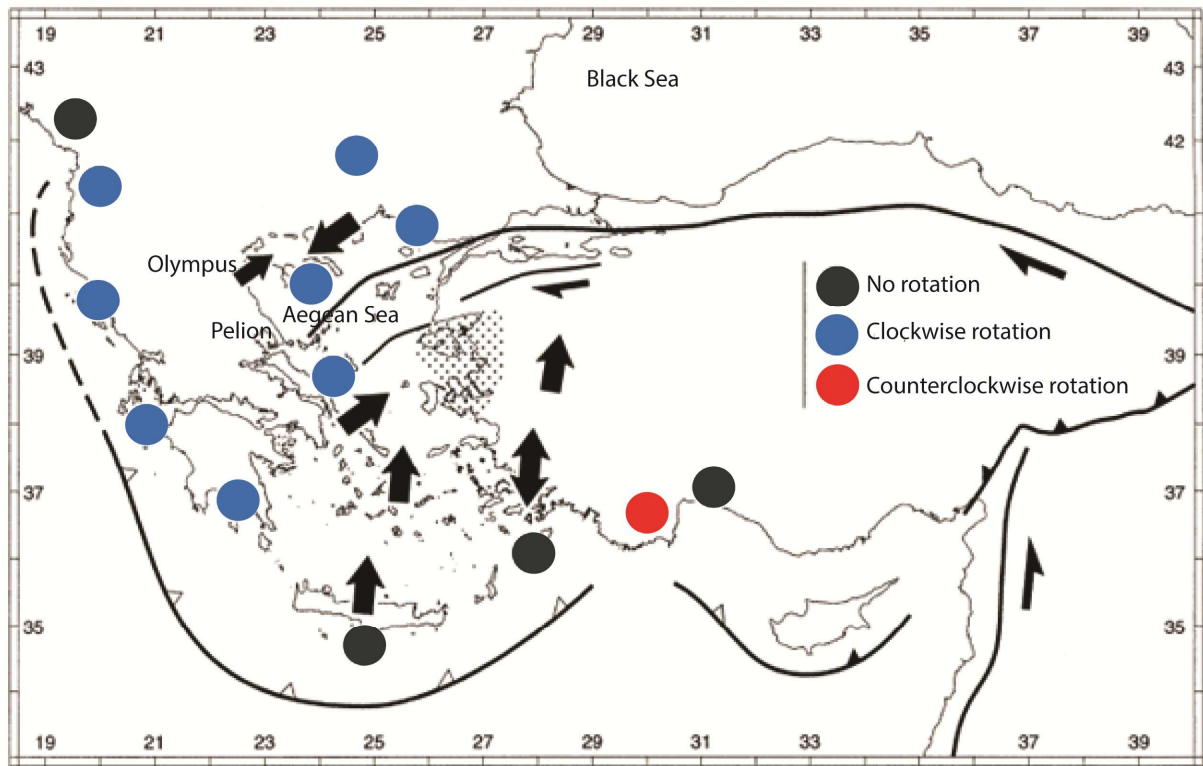
Figure 8: Map showing relationship between extensional deformation direction (dark arrows) and paleomagnetic rotation data (Circles) (Modified from Gautier et al., 1999).

Chapter 3 – Methodology

3.1 – Introduction to low-temperature thermochronology

Thermochronology is a discipline relying on radiometric dating with an understanding of the diffusive transport of daughter isotopes in minerals in response to temperature conditions. It is therefore used to reconstruct the thermal evolution of mineral and rocks in order to constrain the temporal and spatial evolution of a number of geologic processes (Reiners et al., 2005, Bargnesi et al., 2012).
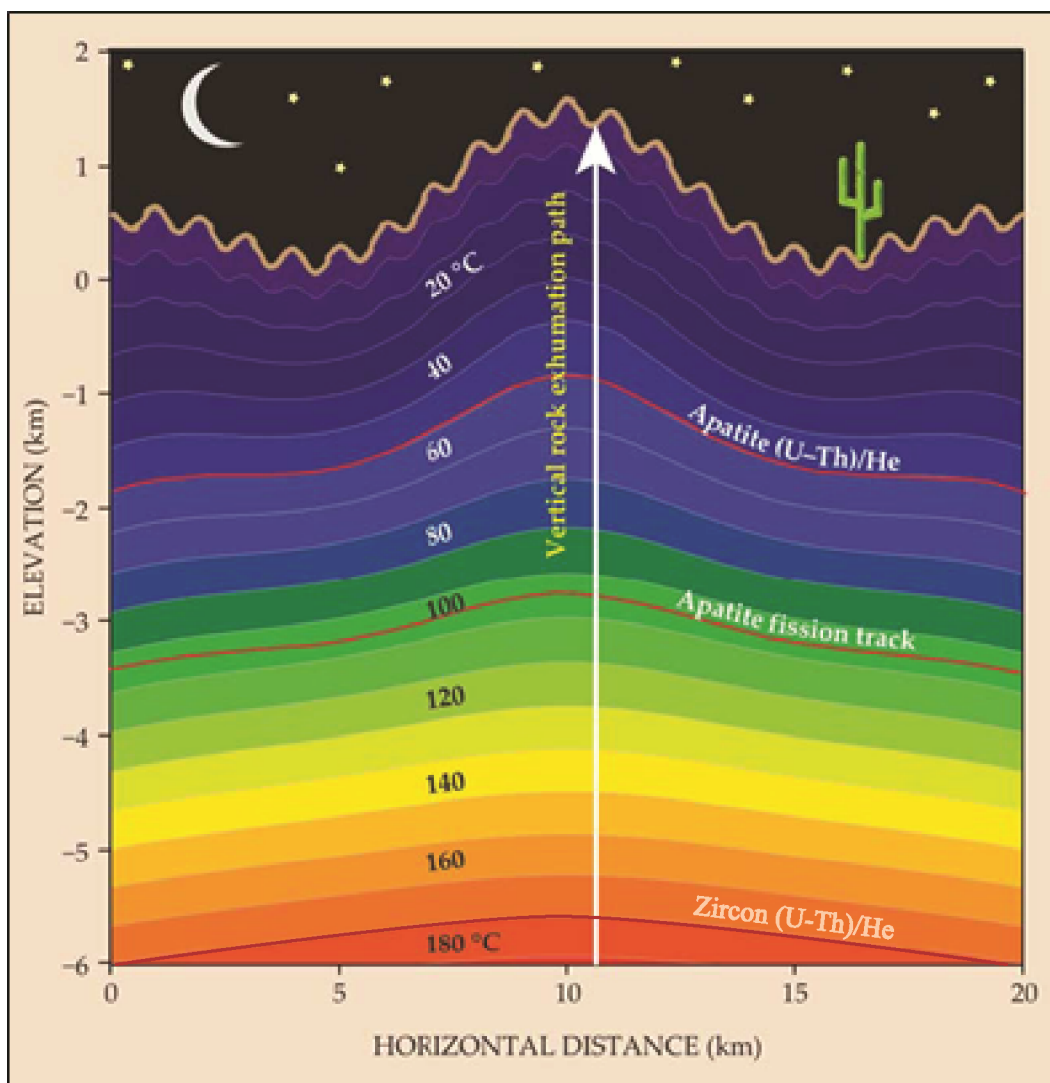
Figure 9: Schematic thermal profile of the upper crust (From Reiners and Shuster, 2009).

Below the Earth's surface, the temperature increases with depth (Fig. 9) to a degree depending on the tectonic and geodynamic setting of a region. For example, the geothermal gradient will be low in stable cratonic regions (10-20°C/km) while it may be much higher in tectonically active mountain ranges (> 40°C/km). When a rock at depth, is displaced toward the surface under the action of surface erosion or by removal of crustal overburden by tectonic processes, i.e. when it is exhumed (England and Molnar, 1990), it will also cool. The cooling rate of an exhuming sample depends on a number of factors affecting the subsurface thermal field (ie. the geometry and the distribution of the isotherms) such as magmatism, fault motion, topography, fluid flow, and erosion (Ehlers, 2005) as well as the rock trajectory within that specific thermal field.

To monitor the cooling of crustal sections, a wide variety of thermochronometers is available and include fission track, (U-Th)/He, $^{39}Ar/^{40}Ar$, and K/Ar dating methods ((Fig. 10). Each thermochronometer is characterized by a different range of temperatures at which diffusion of the daughter isotopes is no longer significant (closure temperature), and combining data from different thermochronometers allows to build a cooling history through different crustal depths (Farley, 2002) and investigate different types of geological processes.
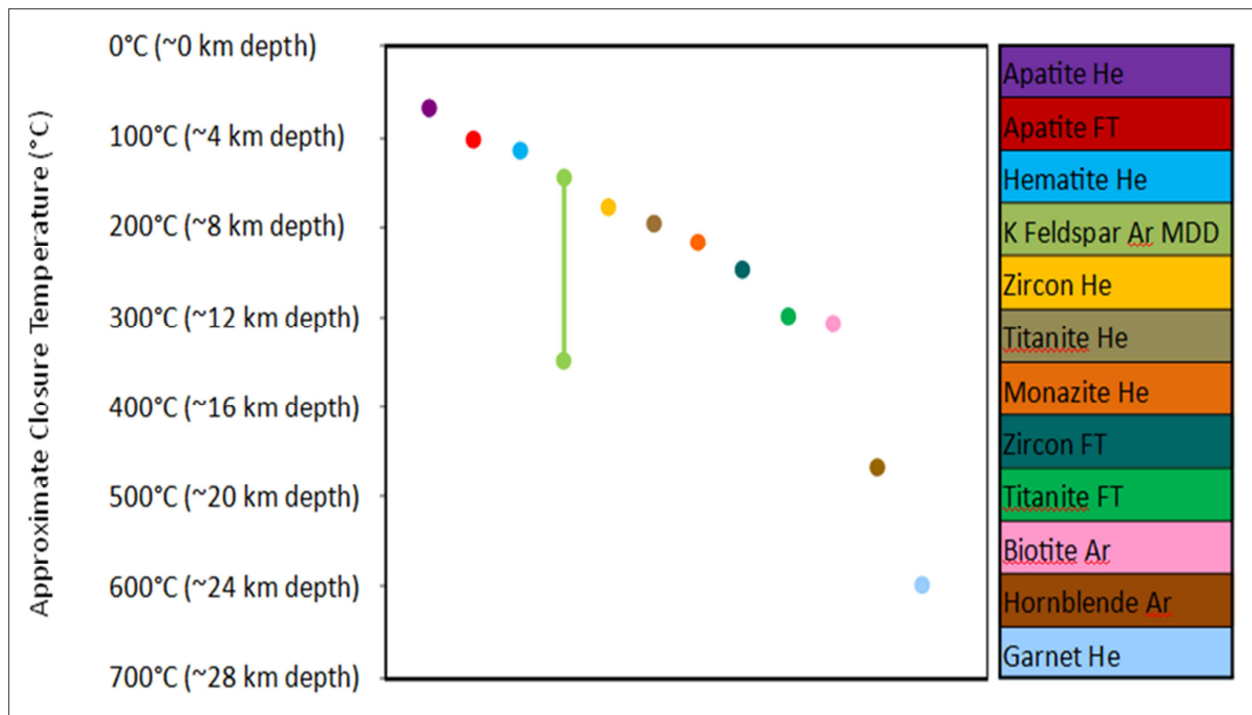
Figure 10: Approximate closure temperatures of various thermochronometers. (Modified from Farley, 2002)

3.2 - Application of Thermochronology to Extensional Tectonic Settings

Extensional tectonic settings such as back-arc basins, passive continental margins, intra-continental extensional provinces, and mid-ocean ridges are dominated by normal faults (Stockli, 2005). As slip occurs along normal faults, rocks once at depth in the footwall move upwards and become tectonically exhumed (Ehlers 2005; Stockli, 2005). This exhumation will displace these rocks from high temperatures deep within the crust, and cool them through the closure temperatures of various thermochronometers on their way to the surface (Fig. 10) (Stockli, 2005; Ehlers, 2005; Farley, 2002). Interpretation of thermochronological data can be complicated by the fact that both erosional and structural processes can lead to crustal cooling (Stockli, 2005). Within extensional settings, thermochronological methods have been used to gain understanding of fault slip rates, timing of extensional onset and duration, magnitude of exhumation, initial fault system geometry, and crustal thermal conditions throughout extensional periods (Stockli, 2005). The magnitude of tectonic exhumation is a function of fault slip, fault

geometry and time. In this study we focus on crustal cooling only, as uncertainties on the geometry of the thermal field configuration at depth prevent us to calculate exhumation rates.
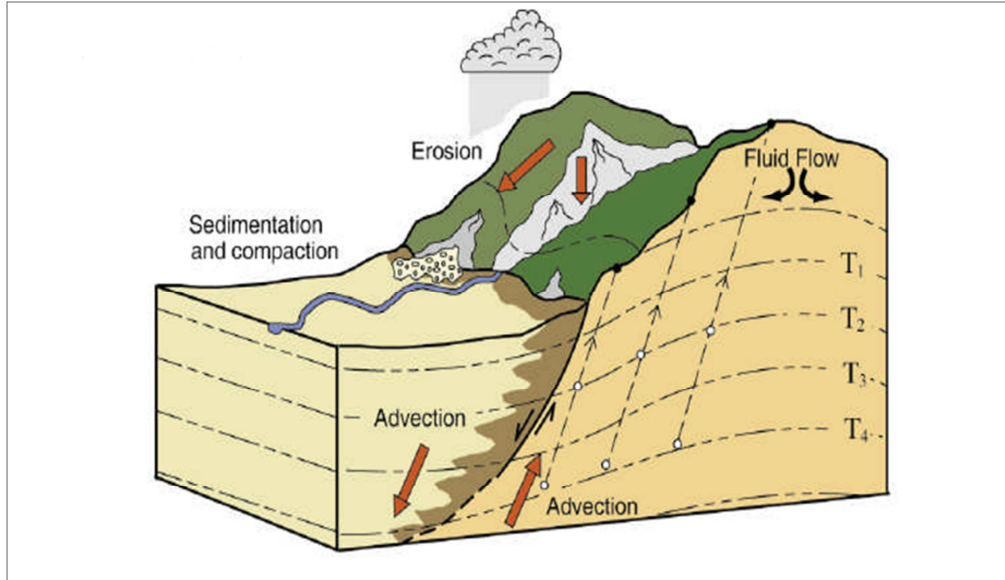
Figure 11: Processes influencing thermochronometer interpretation in an extensional setting. Dashed lines show isotherms of increasing temperature with depth. White circles show the projected particle path during exhumation (From Ehlers, 2005).

High-angle normal faults and low-angle normal faults (also known as low-angle detachment faults) are the two end-member types of extensional faults (Stockli, 2005). High-angle normal faults have an initial dip of ~60°, and can be further divided into rotational or non-rotational, and planar or listric (Stockli, 2005). High-angle normal faults can root at depth on other high-angle or low angle normal faults, or on ductile shear zones, and removal of the hanging wall can cause isostatic rebound and subsequent rotation of the footwall rocks (Fig. 12) (Stockli, 2005). Low-angle detachment faults have a dip of ~10-35°, commonly exhumes mid-crustal rocks, and can form metamorphic core complexes (Stockli, 2005). The geometry of faulting plays an important role on the magnitude of exhumation because it dictates particle trajectory through the crust; For a similar amount of crustal extension, high-angle normal faults will exhume rocks from a greater depth than low-angle detachment faults. For this reason, low-angle detachment faults can be effective for accommodating large amounts of regional extension. Caution must be exercised

when interpreting thermochronological data in such tectonic setting, because there may be a delay in the cooling of a sample following normal faulting, due to the advection of heat in the footwall inducing the compression of isotherms during exhumation (Stockli, 2005). Furthermore, because (U-Th)/He data are a function of cooling rate, partial diffusive loss of He (the daughter product) in the Partial Retention Zone (PRZ, temperature range within which Helium partially diffuses outside of the crystal) must be considered before interpreting when a sample cooled through a specific closure temperature (Stockli, 2005).

As previously discussed, the Olympus-Ossa massifs are tectonic windows located in the footwall of a high-angle normal Aegean fault (e.g. Nance, 2009). I have processed 16 bedrock samples from within the footwall of the Aegean fault for apatite and zircon (U-Th)/He thermochronology in order to constrain the cooling history of the Olympus-Ossa massif.
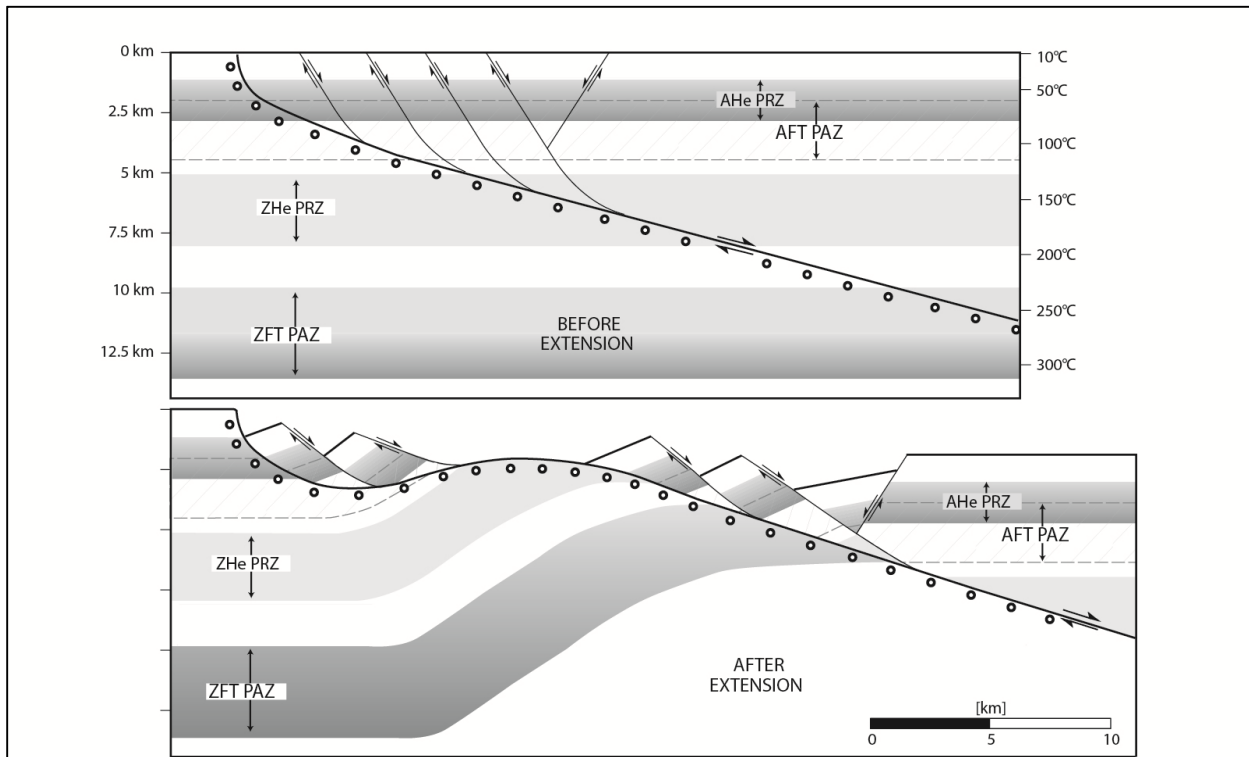
Figure 12. Conceptual model illustrating exhumation of footwall rocks beneath low-angle normal faults. High-angle normal faults are connected to low-angle detachment fault at depth, and isostatic rebound of the footwall is shown. Ideal footwall sampling locations (small circles) are shown before and after exhumation. Bottom graph plots when the various thermochronometers would be expected to cross its closure temperature (From Stockli, 2005). Abbreviations

used - PRZ: partial retention zone; PAZ: partial annealing zone; AHe: apatite helium; ZHe, zircon helium; AFT: apatite fission track; ZFT: zircon fission track.

3.3 - Selection of sample locations

Samples were collected along an SW-NE trending transect, perpendicular to the main structures, crosscutting the different lithological units of the footwall with a denser sampling within and around tectonic windows of Mount Olympus and Mount Ossa (Fig. 3) (Table 1). Samples were collected by Isabelle Coutand in 2011. Samples within the tectonic windows were limited by lithology. The Olympus Ossa unit is nearly exclusively marbles which do not yield zircons or apatites, so whenever available, samples were selected from Pindos flyschs found within the tectonic windows. No samples were collected from the hanging-wall, as it lies offshore, in the Thermaikos gulf.

3.4 - Sample preparation

Prior to the commencement on my project, the samples were separated using standard mineral separation procedures. The selection of apatite and zircon grains was performed at the Thermochronology Laboratory at Dalhousie University. The pre-separated grains were sieved to 104 - 250 μm and evaluated under a stereoscopic microscope. 23 rock samples were analysed and 50 grains of each mineral were selected with geometries best representing tetragonal prisms, or oblate spheroids if tetragonal prisms were not found. From each of these sets of 50 grains, 5 aliquots were selected using a stereoscopic microscope equipped with transmitted, reflected and polarized light. Grains containing fluid and mineral inclusions were rejected for reasons which will be discussed in this chapter. The petrographic microscope was connected to the computer software Pax-It, which allowed precise measurements of the size of each grain in three directions and the diameter of terminal prisms.

From the initial 23 rock samples investigated, only 13 provided grains suitable for dating, including 10 zircon samples, and 6 apatite samples Each aliquot was then sealed in Niobium tubes, ready for the next step of the procedure which involves He, U and Th measurement. This

stage was completed at the University of California in Santa Cruz, by Bertha Louis (operator) under the supervision of Jeremy Hourigan, Assistant Professor in the Department of Earth and Planetary Sciences and director of the (U-Th)/He laboratory.

Table 1. Summary of Grain Description

Samples	Location / Unit	X - Axis	Y - Axis	Z - Axis	Pyramid 1	Pyramid 2	Geometry and Inclusion notes
		mm	mm	mm	mm	mm	
PEL01-2011-ZR1	39°53'19.43"N	280.3	141.9	124.8	36.13	36.31	Tetragonal prism, 2 pyramids, no inclusions
PEL01-2011-ZR2	22°13'45.88"E	260.2	87.21	86.8	34.37	32.52	Tetragonal prism, 2 pyramids, no inclusions, (pyramids are irregularly shaped, see photo Y)
PEL01-2011-ZR3	Pelagonian	258.5	124.7	115.7	39.79	38.11	Tetragonal prism, 2 pyramids no inclusions,
PEL01-2011-ZR5		278.3	123.3	111.4	36.18	30.77	Tetragonal prism, 2 pyramids, seemingly great number of very small solid inclusions, many internal visual imperfections
PEL01-2011-ZR6		325.3	128.6	122.9	48.91	47.01	Tetragonal prism, 2 pyramids, seemingly great number of very small solid inclusions, many internal visual imperfections
PEL02-2011-AP1	39°47'19.18"N	200.5	124.7	90.33	0	0	Cylindrical, no pyramids, no inclusions
PEL02-2011-AP3	22° 1'1.92"E	225.9	153.6	122.9	0	0	Cylindrical, no pyramids, several very small inclusions (Clean break in two during repacking in niobium)
PEL02-2011-AP4	Pelagonian	178.9	133.7	95.77	0	0	Cylindrical, no pyramids, no inclusions, one end is roughly broken
PEL02-2011-AP5		233.1	113.8	103	0	0	Cylindrical, no pyramids, one small & one very small solid inclusion (clean break in two during repacking in niobium)
PEL02-2011-ZR1	39°47'19.18"N	241	115.7	106.7	41.91	32.57	Tetragonal prism, 2 pyramids, no inclusions, one large fracture
PEL02-2011-ZR2	22° 1'1.92"E	217.4	128.5	99.78	30.93	30.77	Tetragonal prism, 2 pyramids moderately eroded, no inclusions
PEL02-2011-ZR3	Pelagonian	197.6	98.16	92.42	36.18	34.33	Tetragonal prism, 2 pyramids, 2 medium size fluid inclusions, 1 med size zr inclusion.
PEL02-2011-ZR4		188	108.6	99.52	23.49	25.29	Tetragonal prism, 2 pyramids, 4 very small solid inclusion,
PEL02-2011-ZR5		314.4	148.4	141.1	54.23	50.62	Tetragonal prism, 2 slightly eroded pyramids, no inclusions
PEL03-2011-AP2	39°46'22.73"N	155.4	131.9	128.3	25.29	0	Hexagonal prism, 1 pyramid heavily eroded, 1 end cleanly broken off, 1 small fluid inclusion, 2 patches show interior imperfections
PEL03-2011-AP3	21°57'13.64"E	178.9	117.5	97.58	19.87	0	Hexagonal prism, 1 pyramid heavily eroded, other pyramid absent, one small solid inclusion (see photo),
PEL03-2011-AP4	Pelagonian	162.6	130.1	124.7	25.29	0	Hexagonal prism, 1 pyramid heavily eroded, other end is cleanly broken off, one medium solid inclusion
PEL03-2011-AP5		204.2	131.9	122.9	23.49	12.78	Hexagonal prism, 2 pyramids heavily eroded, one small solid inclusion
PEL03-2011-AP6		156.1	111.8	104.7	21.15	18.86	Hexagonal prism, 2 pyramids heavily eroded, one small solid inclusion
PEL03-2011-ZR1	39°46'22.73"N	325.2	117.5	106.8	87.19	74.07	Tetragonal prism, 2 pyramids, no inclusions, one small interior fracture
PEL03-2011-ZR3	21°57'13.64"E	310.8	128.7	126.5	52.42	50.88	Tetragonal prism, 2 pyramids, no inclusions, 4 or 5 interior fractures.
PEL03-2011-ZR5	Pelagonian	273	92.16	84.99	36.13	23.49	Tetragonal prism, 2 pyramids, 2 small solid inclusions, interior visual imperfections
PEL03-2011-ZR6		287.3	104.8	92.16	61.45	34.37	Tetragonal prism, 2 pyramids, 1 medium solid inclusion, 2 small solid inclusions, internal visual imperfections

Sample	Coordinates	Region						Description
PEL03-2011-ZR8			316.2	113.9	101.2	77.71	72.47	Tetragonal prism, 2 pyramids, 2 very small and 1 small solid inclusions
PEL03-ZR1	39°48'36.12"N		287.4	112	95.75	39.91	51.1	Tetragonal prism, 2 pyramids, no inclusions, minor interior visual imperfections
PEL03-ZR2	22° 2'7.98"E		285.7	93.96	81.32	41.59	36.13	Tetragonal prism, 2 pyramids, no inclusions, minor interior visual imperfections
PEL03-ZR3		Pelagonian	294.8	88.69	68.75	23.49	25.29	Tetragonal prism, 2 pyramids, 1 medium sized solid inclusion, minor internal visual imperfections
PEL03-ZR4			242.2	86.74	72.29	30.71	19.87	Tetragonal prism, 2 pyramids, no inclusions, minor interior visual imperfections
PEL03-ZR5			240.3	83.11	81.3	25.36	23.56	Tetragonal prism, 2 pyramids, 1 med solid inclusion, minor interior visual imperfections
OLY01-2011-ZR1	40° 7'25.54"N		245.8	121.1	76.07	36.31	47.11	Tetragonal prism, 2 pyramids moderately eroded, 3 small fluid inclusions,
OLY01-2011-ZR2	22°17'8.34"E		251.9	94.38	92.21	37.25	32.97	Tetragonal prism, no inclusions, 2 pyramids moderately eroded.
OLY01-2011-ZR3	Olympus/Ossa		273.4	127.8	104.6	43.51	45.31	Tetragonal prism, 2 pyramids, no inclusions,
OLY01-2011-ZR4	(Pindos)		311.6	94.38	90.78	45.49	45.31	Tetragonal prism, 2 pyramids slightly eroded, no inclusions
OLY01-2011-ZR5			303.6	101.3	97.58	56.04	68.75	Tetragonal prism, 2 pyramids slightly eroded, one small fluid inclusion,
OLY06-AP2	40° 6'13.08"N		122.9	121.1	108.4	19.96	0	Hexagonal prism, 1 pyramid heavily eroded, other end cleanly broken, no inclusions
OLY06-AP4	22°14'31.92"E		186.1	115.6	93.96	0	0	Hexagonal prism, no pyramids, one end roughly broken, 1 very small solid inclusion
OLY06-AP5	Ambelakia		150	92.16	90.35	21.68	27.1	Hexagonal, two pyramids highly eroded, no inclusions, minor internal visual imperfections
OLY07-ZR1	40° 1'56.04"N		236.7	115.6	92.16	45.2	63.23	Tetragonal prism, 2 pyramids moderately eroded,no inclusions,
OLY07-ZR2	22°18'49.08"E		216.9	97.58	93.96	61.43	56.27	Tetragonal prism, 2 pyramids slightly eroded,no inclusions, internal visual imperfections
OLY07-ZR3	Olympus/Ossa		198.7	137.4	101.2	50.59	43.51	Tetragonal prism, 2 pyramids slightly eroded, no inclusions,
OLY07-ZR4	(Pindos)		197	115.6	97.58			Elipsoid, few very small solid inclusions, sub round,
OLY07-ZR5			197	130.1	104.9	39.75	30.71	Tetragonal prism, 2 pyramids highly eroded, no inclusions,
OLY09-AP1	40° 0'47.76"N		258.4	97.56	90.33	21.68	0	Hexagonal prism, 1 pyramid highly eroded, no inclusions, (sides highly eroded - cylindrical shaped centre)
OLY09-AP2	22°18'8.28"E		207.8	122.9	113.8	30.71	0	Hexagonal prism, one pyramid highly eroded, other end broken off, no inclusions
OLY09-AP3	Pelagonian		227.7	112	104.8	39.79	21.76	Hexagonal prism, 2 pyramids highly eroded, no inclusions
OLY09-AP5			200.6	106.6	93.96	0	0	Cylindrical shape, no pyramids, no inclusions
OLY09-AP6			160.8	117.5	117.5	19.87	0	Hexagonal prism, 1 pyramid moderately eroded, other end broken off cleanly, no inclusions
OLY09-ZR1	40° 0'47.76"N		232.3	96.04	79.76	32.01	25.55	Tetragonal prism, 2 pyramids, one very small solid inclusion. Two fractures visible within grain.
OLY09-ZR3	22°18'8.28"E		222.1	86.8	86.72	70.48	39.79	Tetragonal prism, 2 pyramids, one very small solid inclusion near pyramid.
OLY09-ZR4	Pelagonian		226.7	98.16	88.55	56.01	45.2	Tetragonal prism, 2 pyramids slighly eroded, no inclusions
OLY09-ZR5			238.5	74.16	70.48	34.52	45.2	Tetragonal prism, 2 pyramids, one fluid inclusion, one small solid inclusion in centre, one visible fracture
OLY09-ZR6			224.3	101.3	87.02	45.31	27.1	Tetragonal prism, 2 pyramids, no fluid or solid inclusions

Sample	Location					Description
OLY10-AP1	40° 0'5.88"N	213.2	108.4	95.77	25.29	0	Hexagonal prism, 1 pyramid highly eroded, 1 very small inclusion (can't tell if solid or fluid)
OLY10-AP2	22°17'48.72"E	195.2	121.1	117.5	21.68	25.29	Hexagonal prism, 2 pyramids moderately eroded, 1 small inclusion (Could be play of light, irregular shape, & no extinction)
OLY10-AP3	Pelagonian	182.5	110.2	104.8	21.76	21.68	Hexagonal prism, 2 pyramids moderately eroded. One interior fracture
OLY10-AP4		157.2	110.2	108.5	28.91	0	Hexagonal prism, 1 pyramid moderately eroded, other end broken off cleanly, one medium fluid inclusion,
OLY10-AP5		227.7	103	97.56	0	0	Hexagonal prism, no pyramids, no inclusions, one large interior fracture
OLY10-ZR1	40° 0'5.88"N	253	104.8	97.56	47.11	34.33	Tetragonal prism,2 pyramids slightly eroded, 3 medium solid inclusions, few small fluid inclusions
OLY10-ZR2	22°17'48.72"E	258.5	103	103	56.04	57.84	Tetragonal prism, 2 pyramids, 2 small solid inclusions,
OLY10-ZR4	Pelagonian	263.8	117.5	117.4	65.07	48.81	Tetra prism, 2 pyramids no inclusions,
OLY10-ZR5		255.2	99.52	95.77	43.7	48.78	Tetragonal prism, 2 pyramids, no inclusions, 2 thick interior fractures
OLY10-ZR6		274.6	103.1	95.77	52.89	36.31	Tetragonal prism, 2 pyramids slightly eroded, 1 very small solid inclusion, interior visual imperfections
OSSA01-2011-AP1	39°45'55.22"N	233.1	160.8	131.9	0	0	Cylindrical shape, no pyramids, 1 small fluid inclusion
OSSA01-2011-AP2	22°35'34.33"E	249.3	142.7	130.1	30.71	21.76	Hexagonal prism, 2 pyramids highly eroded, no inclusions
OSSA01-2011-AP3	Pelagonian	202.4	139.1	124.7	0	0	Elipsoid, no inclusions, interior visual imperfections,
OSSA01-2011-AP4		202.4	135.6	93.95	30.71	0	Hexagonal prism, 1 pyramid highly eroded, one medium sized solid inclusion
OSSA01-2011-AP6		171.6	119.3	115.6	0	0	Elipsoid, 3 very small solid inclusions, subround
OSSA03-2011-ZR1	39°47'33.68"N	247.8	97.56	75.9	43.51	41.91	Tetragonal prism, 2 pyramids moderately eroded, 2 large solid inclusions, few small fluid inclusions
OSSA03-2011-ZR2	22°38'10.03"E	254.8	119.3	99.38	46.97	34.37	Tetragonal prism, 2 pyramids, no inclusions,
OSSA03-2011-ZR3	Olympus/Ossa	208.1	119.3	115.6	45.2	32.52	Tetragonal prism, 2 pyramids highly eroded, no inclusions
OSSA03-2011-ZR4	(Pindos)	240.3	119.3	113.8	0	0	Elipsoid, No inclusions, sub round,
OSSA03-2011-ZR5		213.2	117.5	74.07	0	0	Elipsoid, No inclusions, sub angular
OSSA04-ZR1	39°47'11.76"N	169.8	84.91	75.97	21.76	23.49	Tetragonal prism, 2 pyramids slightly eroded, 1 medium and 3 small solid inclusions
OSSA04-ZR2	22°37'25.92"E	164.4	93.96	70.46	0	0	Ellipsoid, no inclusions, subround, interior visual imperfections
OSSA04-ZR3	Olympus/Ossa	151.8	70.46	66.87	0	0	Ellipsoid, no inclusions, subround,
OSSA04-ZR4	(Pindos)	144.6	70.48	68.68	25.29	25.29	Tetragonal prism, 2 pyramids moderately eroded, 1 small solid (maybe fluid) inclusion
OSSA04-ZR5		155.4	75.88	63.23	21.68	21.68	Tetragonal prism, 2 pyramids highly eroded, no inclusions, interior visual imperfections

3.4.5 (U-Th)/He thermochronology

(U-Th)/He thermochronometry relies on the accumulation of ^{4}He (α particles) from the radioactive decay of ^{238}U, ^{235}U, and ^{232}Th within apatite and zircon crystals (Farley, 2002; Hourigan et al., 2005). ^{4}He is retained in the grain when located below its closure temperature (Tc) and completely lost from the grain through thermally-activated diffusion when submitted to temperatures higher than Tc (Farley, 2002; Reiners and Brandon, 2006).

3.5.1 - Principles of the method and age calculation

3.5.1.1. Helium ingrowth

α-particles (^{4}He) are produced by the decay of ^{238}U, ^{235}U, and ^{232}Th, and in a lesser proportion, by α decay of ^{147}Sm (Farley, 2002; Reiners, 2005). In almost all minerals, radiogenic ^{4}He from ^{147}Sm is negligible so the ^{4}He ingrowth equation is:

$$He = 8\ ^{238}U\ (e^{\lambda 238 t} - 1) + 7\ ^{238}U\ (1/137.88)\ (e^{\ \lambda 235 t} - 1) + 6\ ^{232}Th\ (e^{\ \lambda 232 t} - 1) \qquad (1)$$

where He, U, Th are present-day abundances of each element, λ is the decay constant (λ_{238} = 1.551 x 10^{-10} yr^{-1}, λ_{235} = 9.849 × 10^{-10} yr^{-1}, λ_{232} = 4.948 × 10^{-11} yr^{-1}), and t is the accumulation time or helium age. The coefficients preceding the abundances for ^{238}U, ^{235}U and ^{232}Th account for the amount of α-particles created from each radioactive parent, and the fraction 1/137.88 is the present day ratio of ^{235}U/^{238}U (Farley, 2002). Equation (1) assumes that there is no initial ^{4}He in the crystal when it starts to cool from above Tc (Farley, 2002), Hence. most of the He accumulated in a mineral did so through radioactive decay only after the mineral cooled below

its Tc (Farley, 2002). However, there exist a number of potential contamination sources. The atmosphere contains He, albeit at low concentration (about 5 ppm), and is unlikely to have any effect on He concentration of the minerals (Farley, 2002). Some fluids from which the minerals grow may contain crustal or mantle-derived helium and that is why grains with detectable fluid inclusions are discarded. However, for U and Th rich minerals such as apatite and zircon, both the concentration of He in fluid and the inclusion density in the crystal would have to be very high to significantly affect the final age (Farley, 2002). Finally, fluids containing He and percolating through crustal material may penetrate into crystals, but no data are as of yet available to evaluate the effect of this process (Farley, 2002).

3.5.1.2. Helium diffusion

At the surface temperature, ^{4}He helium is retained in apatite and zircon, but at depth it diffuses out of the crystals as fast as it is being produced (Farley, 2002; Hourigan et al., 2005; Reiners and Brandon, 2006). Diffusional loss in apatite below temperatures of 300°C is controlled by the Arrhenius relationship:

$$(D/a^2) = (D_0/a^2) \, e^{-Ea/RT} \tag{2}$$

Where D is the diffusivity, D_0 is the diffusivity at an infinite temperature, a is the radius of the diffusion domain (the crystal prism radium), E_a is the activation energy (between 32 and 38 kcal/mol), and R is the gas constant (Farley, 2002; Reiners and Brandon, 2006).

Diffusional loss in zircon does not follow the Arrhenius relationship (Farley, 2002). Differences from apatite diffusion include a strong zonation of U and Th, and radiation damage in zircons promotes He loss above temperatures 250°C (Farley, 2002).

The temperature at which helium retention begins to outpace diffusion is at the base of a temperature range called the Partial Retention Zone (PRZ), and the top of the PRZ is where 90% of He is retained (Fig. 13) (Farley, 2002; Reiners and Brandon, 2006). Closure temperatures for AHe and ZHe dating are defined as the temperature at the base of the PRZ (Farley, 2002; Reiners and Brandon). Laboratory diffusion experiments suggest that the closure temperature for apatite is 70°C, and 180°C for zircon, but this temperature varies depending on the grain size and the cooling rate (Fig. 14) (Farley, 2002; Reiners, 2005).
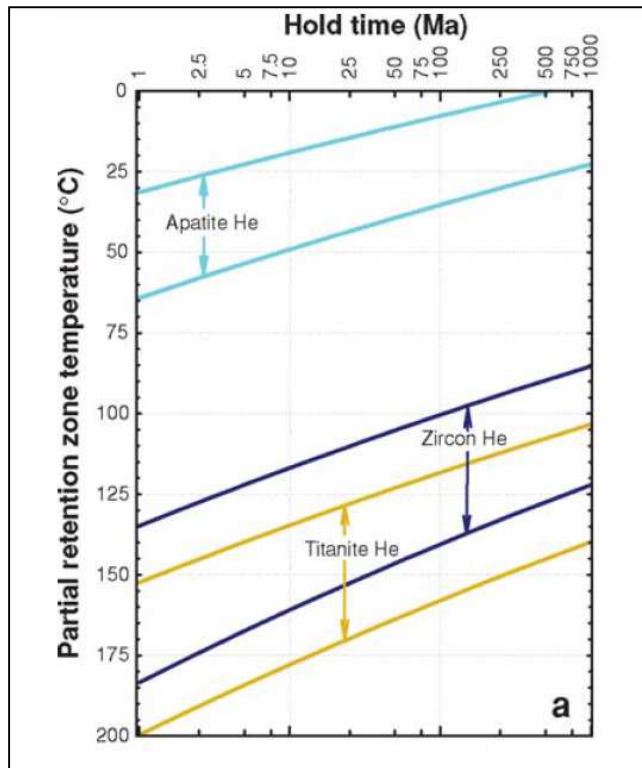

Figure 13: Loss-only partial retention zones (PRZs) for He thermochronometers. The PRZ is defined by upper and lower boundaries, indicating 90% and 10% retention, repectively, after being held at a steady temperature for a specified amount of time (Hold time) (From Reiners and Brandon, 2006).
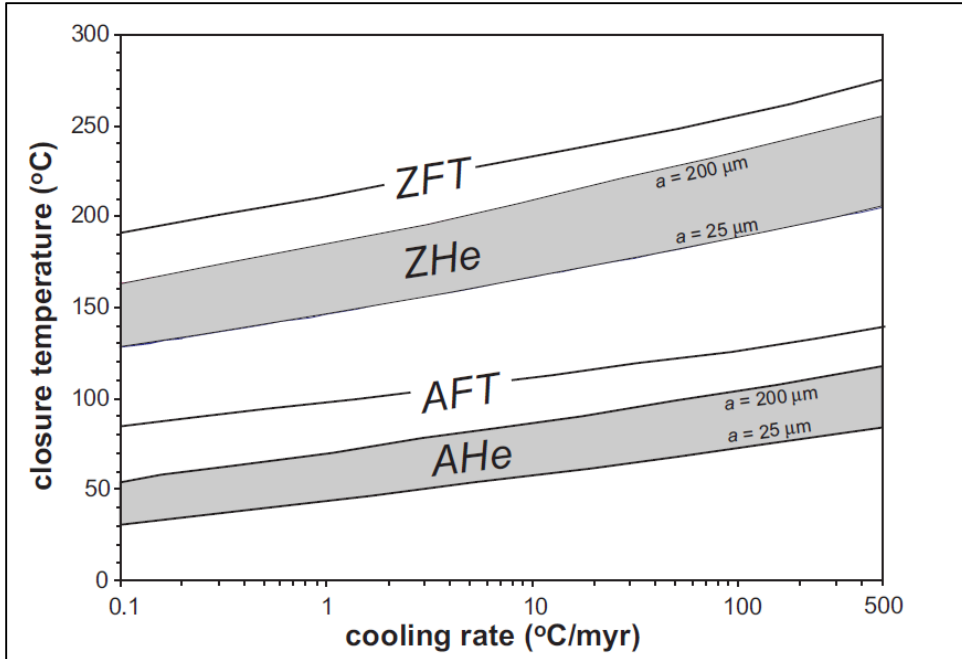
Figure 14: Closing temperatures for AHe and ZHe systems as a function of cooling rate and crystal size (From Reiners, 2005).

3.5.2. - α-particle ejection and correction

α-particles emitted from the series decay of U and Th have enough kinetic energy to travel approximately 20 μm through the crystal lattice before coming to rest (Farley, 2002; Hourigan et al., 2005). If the radioactive parent is not homogenously distributed within the crystal, this can lead to local variability in parent/daughter ratios, age heterogeneity within the rock, and erroneous ages if not accounted for (Farley, 2002; Hourigan et al., 2005). The stopping distance can lead to three relevant outcomes of α-emission: retention, ejection, and implantation (Fig. 15) (Farley, 2002). When α-emission occurs on the outer edge of the grain, the probability of ejection rises to a maximum of almost 50%, and this probability lowers to zero as the distance to the grain edge is over 20 μm (Farley, 2002).This phenomena needs to be accounted for because it bias the finite He content of crystals and consequently may modify the cooling age.
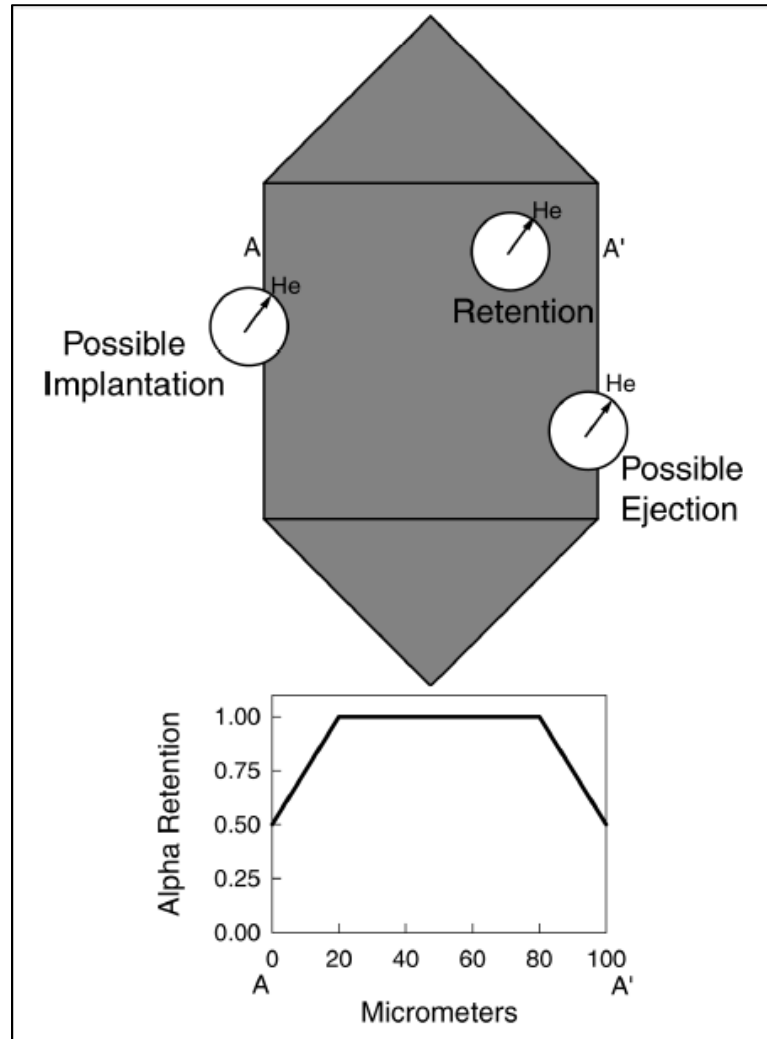
Figure 15: Three possible outcomes of alpha ejection (From Farley, 2002)

The effect of α-ejection can be corrected by chemical or mechanical removal of the outer 20 μm of the grain, however the margin is also the site of increased diffusional loss and this will bias the sample towards higher He abundance (Farley, 2002). To overcome this obstacle, Farley et al (1996) developed a model for correcting He ages based on grain sizes and geometry (Farley, 2002). The implementation of this model requires grains to be selected based on specific geometry, because the correction requires surface area and volume calculations (Fig. 16, Table 2) (Farley, 2002). The selected grain lengths and prism diameters are measured and a α-ejection corrected age is then calculated (Farley, 2002; Reiners, 2005).
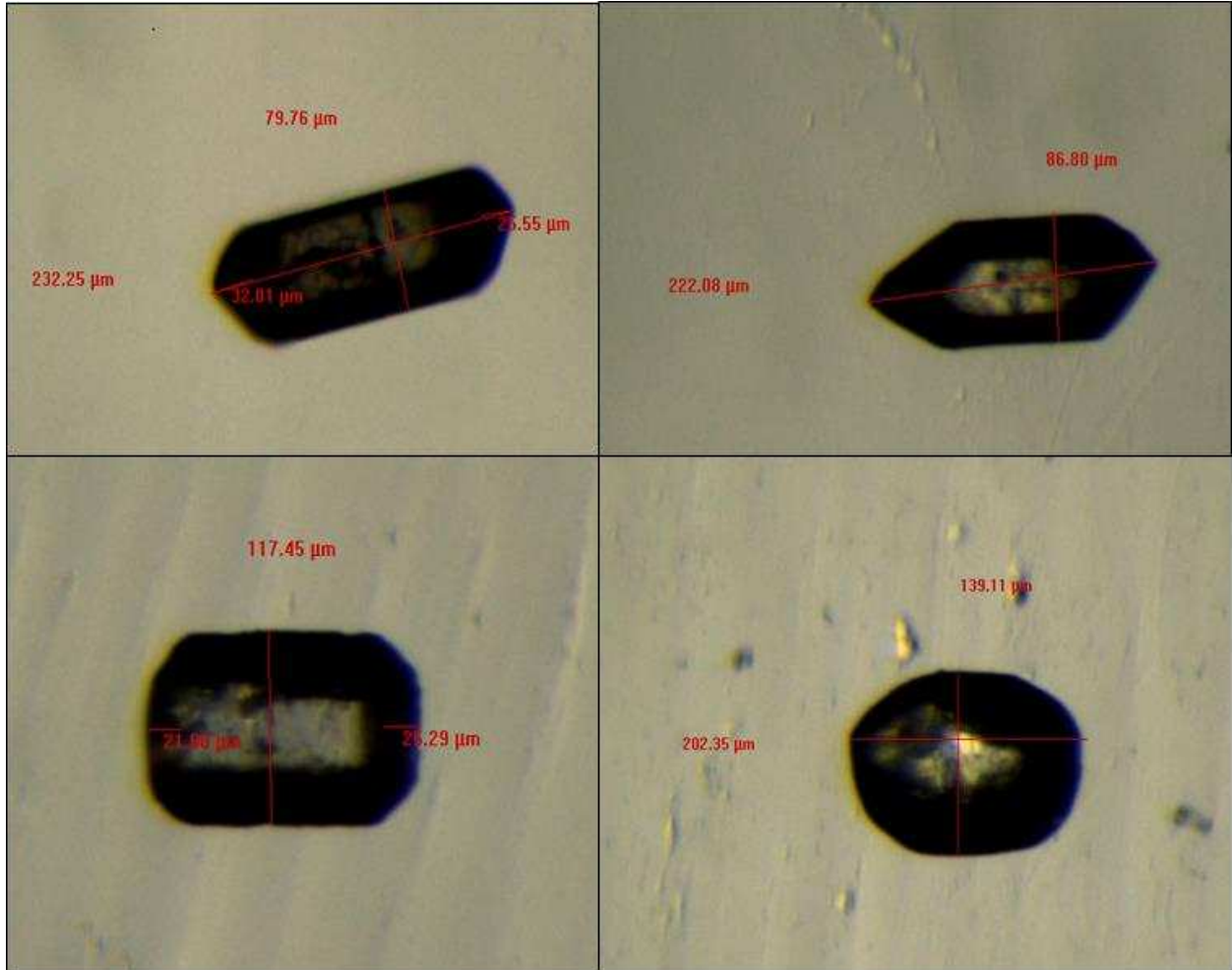
Figure 16: Examples of grain geometries from sample grains selected for this study. Clockwise from top left: OLY 09 ZR1, OLY09 ZR3, OLY10 AP2, OSSA01-2011 AP3. Photos taken with PAX-IT software connected to stereoscopic microscope under transmitted light. Zircons at the top show tetragonal prism geometry with well-defined peaks. The apatites at the bottom show hexagonal prism with peaks moderately eroded (left), and ellipsoid geometry (right).

α-ejection corrections for zircon grains are determined by calculating the fraction of He retained in crystals (F_{He}) from the equation

$$F_{He} = 1 + A_1\beta + A_2\beta^2 \tag{3}$$

where A1 and A2 are given for different morphologies, and β is the surface area to volume ratio (Table 2) (Reiners, 2005).

| | Tetrahedral prism with pinacoidal terminations | | | | Tetrahedral prism with pyramidal terminations | |
| | (Farley 2002) | | (Hourigan et al. 2005) | | (Hourigan et al. 2005) | |
Parent Nuclide	A_1	A_2	A_1	A_2	A_1	A_2
^{238}U	−4.31	4.92	−4.35	5.47	−4.28	4.37
^{232}Th	−5.00	6.80	−4.94	6.88	−4.87	5.61

Table 2: Factors A1 and A2 for calculating the fraction of He retained in zircon crystals for different crystal geometries .(from Reiners, 2005).

Geometry	Volume	Surface Area
Tetragonal* prism with pyramidal terminations	$V_z = 4\,r_1 r_2\left[(l - h_1 - h_2) + \dfrac{1}{3}(h_1 + h_2)\right]$	$SA_z = 4(l - h_1 - h_2)(r_1 + r_2) + 2r_1 a + 2r_2 b$ $a = \sqrt{h_1^2 + r_2^2} + \sqrt{h_2^2 + r_2^2}$ $b = \sqrt{h_1^2 + r_1^2} + \sqrt{h_2^2 + r_1^2}$
Prolate Spheroid	$V_{ps} = \dfrac{2}{3}\pi r^2 l$	$SA_{ps} = 2\pi r^2 + \left[\dfrac{2\pi r \left(\frac{l}{2}\right)^2}{\sqrt{\left(\frac{l}{2}\right)^2 - r^2}}\right]\sin^{-1}\left[\dfrac{\sqrt{\left(\frac{l}{2}\right)^2 - r^2}}{\left(\frac{l}{2}\right)}\right]$

Note: l = c-axis-parallel length; h_1, h_2 = pyramidal termination lengths; r_1, r_2 = mutually-perpendicular prism half-widths or average equatorial radius. Prolate spheroid geometry was not modeled for independent polynomial factors, and is assumed to have the same A's as the tetragonal prism with pyramidal terminations.

Table 3:, Surface areas and volumes of zircons for assumed geometries of zircon crystals. Similar equations can be found for apatite crystals and in Ketcham et al., 2011 (from Reiners, 2005).

A weighted mean F_{He} is then derived by applying the F_{He} to the measured U and Th in the sample using the equations:

$$^{Mean}F_{He} = a_{238}\,^{238U}F_{He} + (1 - a_{238})^{232Th}F_{He} \qquad (4)$$

where a_{238} is the fraction of ^4He derived from U^{238},

and

$$a_{238} = (1.04 + 0.245(Th/U)^{-1} \qquad (5)$$

Once $^{Mean}F_{He}$ is determined, the measured age is divided by the $^{Mean}F_{He}$ to obtain the final age corrected for α-ejection (Farley, 2002; Reiners, 2005).

This approach assumes a uniform distribution of parent nuclides; however zoning maybe common in zircons and to a lesser extent in apatite (Farley, 2002; Reiners, 2005). Zircon grains enriched with U and Th in their core produce ages that are "too old", whereas enriched rims can produce ages that are "too young" (Reiners, 2005). Hourigan et al. (2005) developed a method to overcome the problem of zonation by depth profiling in one-dimensional core-to-rim laser ablation pits each grain selected for dating (Reiners, 2005; Hourigan et al., 2005).

3.5.3. Analytical procedures

3.5.3.1. Helium measurement

Laser extraction has been adapted for helium measurement in zircon and apatite grains, however, laser heating can cause volatilization and loss of U and Th from the sample at the most intensely heated section (Farley, 2002). This loss is presumably to vapour and the elements will be deposited elsewhere within the vacuum chamber and be lost for measurement (Farley, 2002). To overcome this problem, the grains are packed in platinum or niobium foils (1 mm x 1 mm). These metals are good thermal conductors and promote uniform heating of the sample during helium degasing (Farley, 2002). The foil is heated by direct lasing at approximately 1000°C for 3 minute extraction intervals (Bertha Louis, personal communication). The extracted gas is spiked with 0.1-1.0 pmol of ^{3}He and measured with a gas-source quadrupole mass spectrometer (Reiners, 2005). This method of heating is faster and produce analytical precision to approximately 2%, however in practice He ages reproduce to about 6% due to natural variability within grain populations (Farley, 2002).

3.5.3.2. Chemical digestion and ^{238}U, ^{235}U, and ^{232}Th measurement

After helium measurements, apatite grains are dissolved in HNO_3, a known amount of ^{230}Th and ^{235}U is added, and diluted with water to the desired volume (Bertha Louis, personal communication; Farley, 2002). Zircon grains undergo a similar procedure, but have a known amount of HF/nitric acid added. (Bertha Louis, Personal communication; Farley, 2002). Abundances of ^{238}U, ^{235}U, and ^{232}Th are then measured by inductively-coupled plasma mass spectrometry (ICP-MS (Bertha Louis, personal communication; Farley, 2002).

3.5.4. Limitations of the method

In the case of apatite, small U-Th rich solid inclusions (like zircon) can pose a significant problem (Farley et al., 2002; Reiners, 2005). Zircon inclusions in apatite are common, and these small zircon crystals can withstand the dissolution conditions utilized for apatite; consequently they do not contribute any U or Th to the analysis. This generates "parentless" He which may yield erroneously old ages (Farley, 2002). Mineral inclusions may also change diffusion behaviour by modifying the ^{4}He concentration gradient, and localization in the rim or core of U and Th bearing mineral inclusions could affect α-ejection distribution (Farley, 2002).

Obtaining an appropriate mineral standard has proved difficult for AHe dating (Farley, 2002). A requirement for a mineral standard is that the mineral must cross the closure temperature for AHe and the independent chronometer at the same time (Farley, 2002). For this a rapidly cooled volcanic rock is normally chosen, however apatite is susceptible to post-eruptive diffusional loss, which can lead to erroneous ages in the mineral standard (Farley, 2002). Durango apatite was used as the standard for this study.

3.6 - Thermal modelling (HeFTy software)

HeFTy is a computer modeling program which predicts AFT ages, track length, (U-Th)/He ages and thermal histories through forward and inverse models (Ketcham, 2005). In this study, we use HeFTy to run inverse models to predict segments of the time-Temperature (t-T) path and use the obtained cooling ages as inputs.

The application of HeFTy in our analysis can reduce uncertainty through analytical interpretation of the data, and is an integral part of the age-temperature approach in our thermochronological investigation (Reiners et al., 2005; Ketcham, 2005; Stockli, 2005).

A forward model predicts the evolution of a thermochronometer for a pre-defined t-T history (Ketcham, 2005). A forward model can be applied in the inverse sense to construct the range of thermal histories possible given measured cooling ages, and an assumed starting condition (Ketcham, 2005). More than one thermal history may be consistent with the measured cooling ages, and therefore a solution to an inverse model is generally a set of thermal histories which all meet predefined parameters (Ketcham, 2005). Modeling the (U-Th)/He system involves computations of alpha production, alpha ejection, and diffusion within the crystal (Ketcham, 2005). For the (U-Th)/He isotopic system, good calibration of diffusion behaviour has been completed for apatite, zircon, and titanite crystals using a series of step-heating experiments (Ketcham, 2005; Reiners, 2005). A large number of techniques have been developed to deal with statistical tests of model predictions, assessing candidate thermal histories, and presenting results (Ketcham, 2005). Before modeling, it is important to evaluate the data to ascertain whether they are of a high enough quality to warrant modeling (Ketcham, 2005). Fitting conditions must be selected prudently, especially with regard to selection of user-imposed constraints on the thermal history (Ketcham, 2005). If (U-Th)/He data show significant zoning, the model should not be run without proper zoning measurements by LA-ICPMS analysis (Ketcham, 2005). Thermal histories should begin at sufficient temperatures to ensure there is no helium in the initial condition, so significantly above the closure temperature of ZHe and the final constraint should be the temperature at which the sample was collected (Ketcham, 2005).

HeFTy allows constraints to be added as a box encompassing a t-T range, and candidate paths are plotted by connecting line segments to randomized points within these boxes (Ketcham, 2005).

Line segments can be straight or split into sub-segments to allow for complexity in the thermal history, although it should be noted that this is not necessarily more accurate (Ketcham, 2005). One argument states that extra degrees of freedom should not be employed if the data can be interpreted using fewer nodes, i.e a "simpler" model (Ketcham, 2005). Opposing arguments state that leaving our extra nodes is to make a potentially erroneous assumption that heating and cooling paths are linear (Ketcham, 2005). If seeking the simplest, single thermal history in a study, fewer degrees of freedom would be preferred (Ketcham, 2005). Allowed complexity is a decision which should be explicitly stated, as it influences the interpretation of the results (Ketcham, 2005). HeFTy allows for this by defining 3 scales of complexity: episodic, intermediate, and gradual. For this study, intermediate has been chosen to reflect potentially rapid cooling events. The segment between constraints was set to monotonic variable, meaning that both cooling and heating paths are allowed provided relevant temperature ranges in the constraints. Segments were halved 2 times without imposing a cooling rate. The ending condition for the Monte Carlo search was set to 10,000 paths for all models created. These paths are evaluated with Kuiper's Statistic to calculate the goodness of fit (GOF) between the measured age and the modelled age (Ketcham, 2013). Paths which produce GOF values > 0.50 are considered to be a "Good" fit, whereas GOF values between 0.50 and 0.05 are considered an "Acceptable" fit (Ketcham, 2013). GOF values on AFT data require not only correlation between the measured and modeled age, but also to cooling rate through Partial Annealing Zone temperatures provided by fission track lengths distribution (Ketcham, 2013). Calibrations for apatites were based on the Durango apatite standard, and calibrations for zircons were based on Reiners et al., 2004. Stopping distances and alpha corrections in HeFTy used values

from Ketcham et al., 2011. HeFTy models were ran on single grain ages, and grains were selected based on closest to the sample mean value for that sample, with standard error of the mean used for the error estimate. HeFTy allows data to be entered as a model of the specified thermochronometer and a time-temperature constraint box to limit random path variability, or just simply as a time-temperature constraint box. Due to unexplained problems with HeFTy modeling functions, some ages were simply entered as just a constraint box. For ZHe and AHe data, this approximation changes little provided the alpha corrected age is used and constraint boxes are kept within 1 σ error of the mean sample age. AFT were entered as a constraint box only in the case where track length data were not available. AHe (and ZHe) constraint boxes were constructed with temperature ranges of 50-90°C (and 160-200°C), in order to keep the centre of the constraint near the closure temperatures of 70°C (and 180°C), while still allowing for changes to the closure temperature as a result of holding time and grain size. The time range for each AHe and ZHe constraint box is the standard error of the mean corrected age for each sample. For AFT data, constraint boxes were constructed with temperature ranges between 100°C and 140°C. A wider range of time was given to constraint boxes for AFT data when entered as a model, given that AFT data have the track length distribution component, and allowing the program flexibility to determine its own course.

Chapter 4 - Results

(U-Th)/He analysis of samples were processed at the University of California Santa Cruz and coupled with unpublished Apatite Fission Track (AFT) data from Coutand et al. (in preparation), to elucidate the low-temperature cooling history of the Olympus–Ossa massif.

AFT data (~120°C closure temperature) show cooling ages of 10.2 ±1.0 -14.3 ± 1.2 Ma for Olympus, 8.5 ± 2 - 10.4 ± 2.2 Ma for Ossa, and 21.9 ± 1.3 - 30.7 ± 2.7 Ma in the Pelagonian zone (for details, see Figs. 3 & 17) (Coutand et al., in preparation).

4.1 - Apatite (U-Th)\He Results

4.1.1. Mount Olympus

Near the Olympus massif, three AHe mean corrected ages were obtained, and listed from north to south these mean corrected ages are 10.6 ± 0.5 Ma, 9.1 ± 2.6 Ma, and 13.1 ± 1.9 Ma reported on OLY06, OLY09 and OLY10, respectively (Table 4). OLY06-AP5 was excluded in the calculation of the mean for OLY06 because the corrected age was tens of millions of years older than other crystals in the sample, and therefore identified as not belonging to the same age population. OLY10-AP1 and AP2 were similarly excluded for ages tens of millions of years older than the main grain population, and in this case could be due to zircon inclusions (Table 1). In sample OLY09, no crystals were excluded from calculation of the mean age. The standard error of the mean for OLY09 is high at 2.6, however this can be reduced to 0.67 by exclusion of aliquots AP1 and AP3 from the calculation of the mean, while reducing the mean age to 8.88 Ma.

4.1.2. Mount Ossa

OSSA01-2011 was the only sample from Ossa which provided suitable material for AHe dating, and gave a mean corrected age of 13.8 ± 1.5 Ma (Table 4). When compared to AFT data for Ossa, this age may seem relatively old, however it is located at the periphery of the tectonic window. The spread of crystal ages in this sample was between 9.6 Ma and 18.5 Ma, and no crystals were excluded from calculation of the mean age. Apatite crystals in this sample were highly eroded, and displayed geometries of ellipsoid, hexagonal prism, and hexagonal prism with peaks and x-axis edges eroded (cylindrical).

4.1.3. Pelagonian Zone

In the Pelagonian zone, mean corrected ages of 13.0 ± 0.8 Ma and 24.5 ± 3.0 Ma were reported on samples PEL02-2011 and PEL03-2011, respectively (Table 2). PEL02-2011-AP4 was identified as not belonging to the same age population as the remaining crystals and was excluded from the calculation of the mean. The geometry of this grain was not as ideal as the remaining grains and this may be the cause of the anomalously old age. PEL03-2011 has a high standard error of the mean corrected ages, and of the 5 aliquots with measured ages only the youngest two, AP2 and AP5, have ages within 10 Ma of each other. These two ages alone were used in calculation of the mean corrected age. Solid inclusions were abundant throughout this sample, and may be the cause of this large spread in ages.

Table 4: Summary of Age
Results

Samples	238U	232Th	147Sm	He	Raw Age	FT: alpha-eject. factor	Corrected Age	Mean Age	Standard Error of the Mean
	mol	mol	mol	mol	Ma		Ma	Ma	Ma
PEL01-2011-ZR1	9.5E-12	4.33621E-12	0	1.022E-11	708.6	0.8549	828.9	245.6	151.9
PEL01-2011-ZR2	7.02941E-11	1.33578E-11	0	2.549E-13	2.7	0.7836	3.4		
PEL01-2011-ZR3	3.60546E-11	8.75E-12	0	3.251E-12	65.8	0.8321	79.0		
PEL01-2011-ZR5	3.24286E-11	4.47845E-12	0	2.133E-12	49.2	0.8320	59.1		
PEL01-2011-ZR6	1.12437E-11	5.89655E-12	0	3.613E-12	218.0	0.8454	257.8		
PEL02-2011-AP1	2.56555E-13	5.96552E-14	0	4.04E-15	11.6	0.8020	14.4	13.0	0.8
PEL02-2011-AP3	1.34832E-13	5.14655E-14	0	2.05E-15	10.8	0.8408	12.9		
PEL02-2011-AP4	1.26387E-13	2.98233E-14	0	3.11E-15	18.1	0.8065	22.4		
PEL02-2011-AP5	2.29622E-13	4.28534E-14	0	2.93E-15	9.5	0.8123	11.7		
PEL02-2011-ZR1	2.18487E-11	2.12198E-12	0	2.237E-12	77.0	0.8202	93.9	53.3	0.9
PEL02-2011-ZR2	4.88235E-12	6.09052E-13	0	2.785E-13	42.8	0.8177	52.3		
PEL02-2011-ZR3	1.37605E-11	1.85819E-12	0	1.93E-14	1.1	0.7875	1.3		
PEL02-2011-ZR4	3.58866E-11	6.51293E-12	0	2.103E-12	43.4	0.8008	54.2		
PEL02-2011-ZR5	6.08824E-11	4.25948E-12	0	5.154E-12	64.2	0.8602	74.6		
PEL03-2011-AP2	2.16933E-13	1.37414E-13	0	5.65E-15	17.6	0.8173	21.5	24.5	3.0
PEL03-2011-AP3	2.07017E-13	1.92241E-13	0	3.36E-14	102.7	0.7990	128.6		
PEL03-2011-AP4	1.89454E-13	6.7069E-14	0	1.43E-14	53.8	0.8190	65.7		
PEL03-2011-AP5	2.8021E-13	4.64224E-14	0	8.6E-15	22.9	0.8309	27.5		
PEL03-2011-AP6	1.45672E-13	6.26293E-14	0	7.21E-15	34.8	0.7956	43.7		
PEL03-2011-ZR1	1.95588E-10	3.33405E-11	0	3.676E-13	1.4	0.8222	1.7	45.1	4.0
PEL03-2011-ZR3	4.93697E-12	1.92284E-12	0	2.085E-12	292.6	0.8471	345.4		
PEL03-2011-ZR5	8.21849E-11	1.4944E-11	0	1.829E-12	16.5	0.7884	21.0		
PEL03-2011-ZR6	2.3416E-11	4.09655E-12	0	1.043E-12	33.1	0.8048	41.1		
PEL03-2011-ZR8	8.90336E-12	2.41078E-12	0	4.918E-13	40.1	0.8161	49.2		
PEL03-ZR1	3.32773E-11	1.58319E-12	0	1.321E-12	30.3	0.8142	37.3	36.3	0.7
PEL03-ZR2	3.19496E-11	1.10129E-12	0	1.187E-12	28.5	0.7875	36.2		
PEL03-ZR3	3.5395E-11	1.03793E-12	0	1.187E-12	25.7	0.7677	33.5		
PEL03-ZR4	3.26639E-11	4.22328E-13	0	1.202E-12	28.3	0.7655	37.0		
PEL03-ZR5	3.31765E-11	5.39224E-13	0	1.246E-12	28.9	0.7732	37.4		
OLY01-2011-ZR1	8.21849E-12	1.26509E-12	0	1.962E-13	17.8	0.7924	22.5	23.1	0.5
OLY01-2011-ZR2	1.43151E-11	1.45431E-12	0	3.375E-13	17.8	0.7949	22.4		
OLY01-2011-ZR3	5.62185E-11	6.84483E-12	0	2.741E-12	36.6	0.8279	44.2		
OLY01-2011-ZR4	2.14664E-11	1.54784E-12	0	5.569E-13	19.7	0.7991	24.7		
OLY01-2011-ZR5	1.11723E-11	2.50647E-12	0	2.776E-13	18.3	0.8058	22.7		
OLY06-AP2	2.37857E-13	5.30603E-13	0	3.67E-15	7.9	0.7809	10.1	10.6	0.5

|									
OLY06-AP4	1.60462E-13	2.82629E-13	0	2.57E-15	8.8	0.7914	11.1		
OLY06-AP5	1.07521E-13	2.44009E-13	0	6.91E-15	32.6	0.7595	43.0		
OLY07-ZR1	1.6979E-11	1.45431E-12	0	5.039E-13	22.5	0.8028	28.0	22.9	0.5
OLY07-ZR2	9.41176E-12	7.68103E-13	0	2.279E-13	18.4	0.7849	23.4		
OLY07-ZR3	1.09748E-11	1.89526E-12	0	2.772E-13	18.8	0.8133	23.1		
OLY07-ZR4	3.88445E-12	6.56897E-13	0	9.905E-14	19.0	0.8033	23.6		
OLY07-ZR5	6.55042E-12	7.90086E-13	0	1.514E-13	17.4	0.8162	21.3		
OLY09-AP1	3.39244E-13	5.34483E-13	0	7.37E-15	12.3	0.7894	15.6	9.1	2.6
OLY09-AP2									
OLY09-AP3	6.07563E-13	1.0319E-12	0	2.64E-15	2.4	0.8076	3.0		
OLY09-AP5	2.66092E-13	3.38319E-13	0	2.88E-15	6.5	0.7902	8.2		
OLY09-AP6	3.68908E-13	8.26724E-13	0	5.53E-15	7.7	0.8017	9.6		
OLY09-ZR1	3.82437E-11	9.26724E-12	0	8.43E-13	16.1	0.7804	20.7	22.0	0.5
OLY09-ZR3	1.30966E-11	5.625E-12	0	3.156E-13	17.0	0.7681	22.1		
OLY09-ZR4	2.06134E-11	4.31466E-12	0	4.939E-13	17.7	0.7856	22.5		
OLY09-ZR5	1.26933E-11	4.13147E-12	0	2.986E-13	16.9	0.7428	22.8		
OLY09-ZR6	5.07563E-11	6.39655E-12	0	7.045E-13	10.4	0.7902	13.2		
OLY10-AP1	1.88151E-13	5.80603E-13	0	8.5E-15	20.4	0.7920	25.8	13.1	1.9
OLY10-AP2	1.93403E-13	3.80474E-13	0	1.08E-14	29.7	0.8147	36.5		
OLY10-AP3	2.64832E-13	7.65948E-13	0	4.72E-15	8.3	0.7949	10.4		
OLY10-AP4	1.64916E-13	5.03448E-13	0	3.42E-15	9.4	0.7877	12.0		
OLY10-AP5	1.69538E-13	4.01164E-13	0	4.5E-15	13.3	0.7924	16.8		
OLY10-ZR1	1.91975E-11	6.92241E-12	0	6.535E-13	24.3	0.8055	30.2	30.2	1.9
OLY10-ZR2	2.12479E-11	2.34871E-12	0	6.807E-13	24.1	0.8070	29.9		
OLY10-ZR4	2.19118E-11	6.84052E-12	0	6.596E-13	21.7	0.8258	26.3		
OLY10-ZR5	2.60042E-11	5.81897E-12	0	7.793E-13	22.0	0.8001	27.5		
OLY10-ZR6	2.12353E-11	8.90086E-12	0	9.03E-13	30.0	0.8049	37.2		
OSSA01-2011-AP1	1.64916E-12	4.26897E-13	0	2.52E-14	11.2	0.8492	13.1	13.8	1.5
OSSA01-2011-AP2	9.5084E-14	7.05603E-14	0	1.84E-15	12.8	0.8442	15.2		
OSSA01-2011-AP3	7.52101E-14	8.47414E-14	0	9.75E-16	8.0	0.8296	9.6		
OSSA01-2011-AP4	7.62605E-14	3.34224E-14	0	1.12E-15	10.3	0.8102	12.7		
OSSA01-2011-AP6	5.53782E-14	3.14009E-14	0	1.21E-15	15.0	0.8101	18.5		
OSSA03-2011-ZR1	2.78739E-11	5.51293E-12	0	7.259E-13	19.3	0.7770	24.8	12.7	1.7
OSSA03-2011-ZR2	2.29034E-12	6.07328E-13	0	2.272E-14	7.2	0.8164	8.9		
OSSA03-2011-ZR3	1.16849E-11	1.83319E-12	0	1.397E-13	8.9	0.8194	10.9		
OSSA03-2011-ZR4	1.76681E-11	1.46767E-12	0	2.831E-13	12.2	0.8243	14.8		
OSSA03-2011-ZR5	1.1937E-11	6.6681E-13	0	1.998E-13	12.8	0.7827	16.3		
OSSA04-ZR1	7.98739E-12	2.09009E-12	0	3.13E-13	28.6	0.7531	37.9	13.2	2.0
OSSA04-ZR2	8.83613E-15	2.76983E-14	0	2.775E-17	1.4	0.7381	1.9		
OSSA04-ZR3	3.71891E-12	2.66552E-13	0	1.035E-13	21.2	0.7151	29.6		
OSSA04-ZR4	5.81513E-12	7.61207E-13	0	6.54E-14	8.5	0.7158	11.8		
OSSA04-ZR5	3.58319E-12	8.94397E-13	0	5.159E-14	10.5	0.7187	14.7		
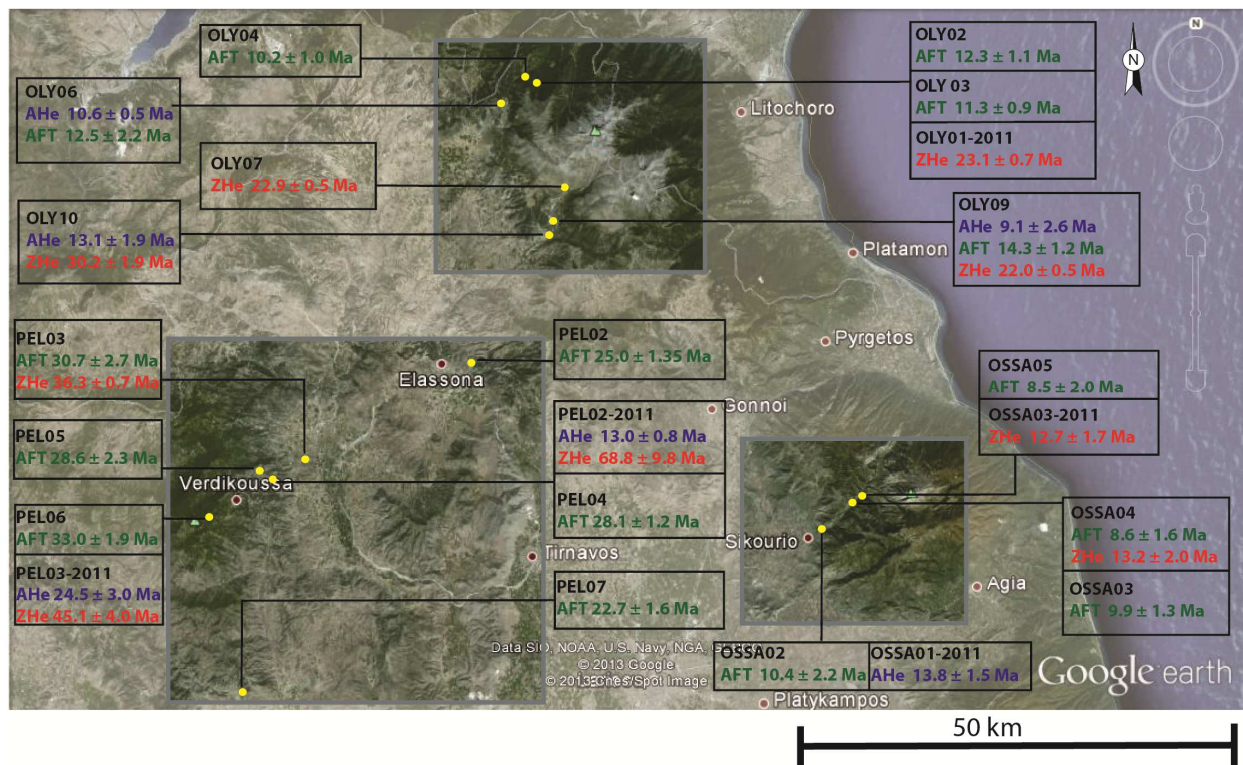
Figure 17: Sample locations with corrected (U-Th)/He and apatite fission track ages. Ages in blue are AHe, ages in green are AFT, ages in red are ZHe. Boxes in grey correspond to sample locations from Figure 2.

4.2 - Zircon (U-Th)/He Results

4.2.1. Mount Olympus

Near the Olympus massif, mean corrected ages of 23.1 ± 0.7 Ma, 22.9 ± 0.5 Ma, 22.0 ± 0.5 Ma, and 30.2 ± 1.9 Ma (Table 4) were reported on samples OLY01-2011, OLY07, OLY09, & OLY 10 respectively. Aliquot ZR3 from OLY01-2011 was excluded from calculation of the mean as the corrected age is tens of millions of years older than the rest of the sample. Similar exclusions for ZHe aliquots in the Olympus sampling region are ZR1 in OLY07, and ZR6 in OLY09. These excluded aliquots show no obvious irregularities which may indicate a reason for their anomalous ages.

The ZHe mean corrected age reported at OLY10 (30.2 Ma) is considerably older than other ZHe samples near Mount Olympus. Being the southernmost of the Olympus group of samples,

and the closest towards the Pelagonian zone, this older age might be expected (as older ages are seen in our Pelagonian samples). However OLY10 lies only ~1.4 km SSW of OLY09, and this may indicate a geographically rapid variance of cooling rates.

4.2.2. Mount Ossa

Samples collected near Ossa recorded ZHe mean corrected ages of 12.7 ± 1.7 Ma and 13.2 ± 2.0 Ma on OSSA03-2001 and OSSA04 respectively (Table 4). In sample OSSA03-2011, aliquot ZR1 was excluded from the calculation of the mean as it was identified as not belonging to the same age population as the rest of the sample due to an older age. A large spread of corrected ages were reported for OSSA04, and only aliquots ZR4 and ZR5 were grouped together to calculate the mean corrected age. 3 of the 5 aliquots were excluded from this calculation because they were identified as not belonging to the same age population. In addition to ages which did not fit with the population, 2 of these excluded crystals had elliptical geometry which does not match the rest of the sample, and the third crystal contained a number of solid inclusions.

4.2.3. Pelagonian Zone

In the Pelagonian zone, samples recorded ZHe mean corrected ages of 36.3 ± 0.7 Ma and 45.1 ± 4.0 Ma on PEL03 and PEL03-2011 respectively (Table 4). In sample PEL03-2011, aliquots ZR1, ZR3 and ZR5 were excluded from calculation of the mean corrected age for not belonging to the same age population as the rest of the sample. Zircon crystals of this sample showed an abundance of solid inclusions and irregular fracturing within the grains. Ages from two other ZHe samples, PEL01-2011 and PEL02-2011, have not been used during analysis due to an older age not fitting with the rest of the sample. While only two ZHe age is available for

Pelagonian regions, they are in agreement of age relationships seen in AFT data: Pelagonian ages are the oldest of the three sample regions.

4.3 - Interpretation of AHe and ZHe results

Single grain ages seen throughout the study samples sometimes show a large dispersion prevent any reliable mean age calculation. Intra-sample age variations can result from a number of causes and two of the more common are parent isotope zonation, and the presence of uranium bearing mineral inclusions (Reiners, 2005). Zoning can affect the age of a sample by causing incorrect alpha ejection corrections. A crystal rim enriched in parent isotopes will lose a large proportion of ^{4}He to ejection, and report ages that are too young, whereas crystals with cores enriched in parent isotope will report ages that are too old (Reiners, 2005). A treatment of zonation in crystals was beyond the scope of this study. Implantation of ^{4}He can also lead to incorrect ages in a similar way as zoning. If adjacent crystals implanted ^{4}He into the sample crystal, it would contain too much ^{4}He and report an age which is too old (Farley, 2002). Variance on grain geometry can have an affect the age of grains, because proper geometry is required for the alpha correction (Reiners et al, 2005; Farley, 2002).
Zircon inclusions in apatite crystals add ^{4}He to the measurements, but they stay intact during chemical digestion of the apatite crystal before ICP-MS measurement of parent U, Th, and Sm isotopes, thus giving an age which is too old due to parentless ^{4}He (Farley, 2002).

Analytical errors associated with the measurement of U, Th, Sm, He, and combined with uncertainty of the alpha ejection correction have not been obtained yet for the study samples. While these analytical errors are generally employed in thermochronologic studies, they do not always accurately predict the reproducibility of ages seen from the same rock due to errors such as those stated above (Meesters and Dunai, 2005). In this study, we have employed the standard error of the mean corrected age, an estimate of how close our sample mean is to the

actual population mean. This choice is conservative since the standard error is usually higher than the analytical error. Because of the common variance of single grain ages discussed above, it is important to remove outliers in the data which do not reflect a coherent age population. Single aliquot ages that are tens to hundreds of years older than others in the same sample were identified as not belonging to the true age population, and were excluded in the calculation of the mean corrected age, and from the standard error of the mean. Presence of these outliers (when not explained by phenomena listed above) maybe due to interferences during isotopes measurements. However, due to the late arrival of the data, we did not yet get the chance to discuss this issue with our collaborator.

4.4. Thermal modelling

Inverse thermal modeling was used to extract 8 thermal histories on samples throughout the 3 lithotectonic domains (Figs. 18-26). The same parameters were selected for each model to ensure consistency and reproducibility of the models (see section 3.5 above). Whenever possible, models incorporate data from AHe, AFT, and ZHe thermochronometers, but this was restricted on the availability of suitable ages. Due to this restriction, samples were grouped together for modeling purposes on a geographic and lithologic basis so that models could reflect a larger thermal history. For example, a single sampling location may have AHe and AFT ages, but no ZHe age. Another sampling location 500 m away may have recorded a ZHe age, and would be included in the model, unless it crossed a tectonic contact.

The model for PEL06 was grouped with PEL03-2011, and generated 10000 paths, of which 3420 were acceptable paths (green), and 915 were good paths (pink) (Figure 18a & Table 5). The first t-T constraint box established in HeFTy was 160°C-200°C / 49-41 Ma on PEL03-2011 ZHe data ran as a constraint box only. The second constraint was 100-140°C / 40-28 Ma on PEL06 AFT ran as a model. The third constraint was 50-90°C / 27.5-21.5 Ma on PEL03-2011

AHe data ran as a constraint box only. The final constraint was a present day temperature range of 15-20°C.

In the thermal model PEL06 / PEL03-2011 we see no discernible pattern around 14-10 Ma which would suggest a cooling event, but just a gradual cooling. However, with the higher AHe date, the model doesn't disprove that a rapid cooling event could have occurred around this time. Since cooling rates are much lower in the Pelagonian than in the tectonic windows, and the possibility that at 14-10 Ma the samples from the Pelagonian were likely at shallow depths where closure temperatures have already been crossed, this cooling event would not be expected to make an impact on the t-T plot as we would expect for the tectonic windows.
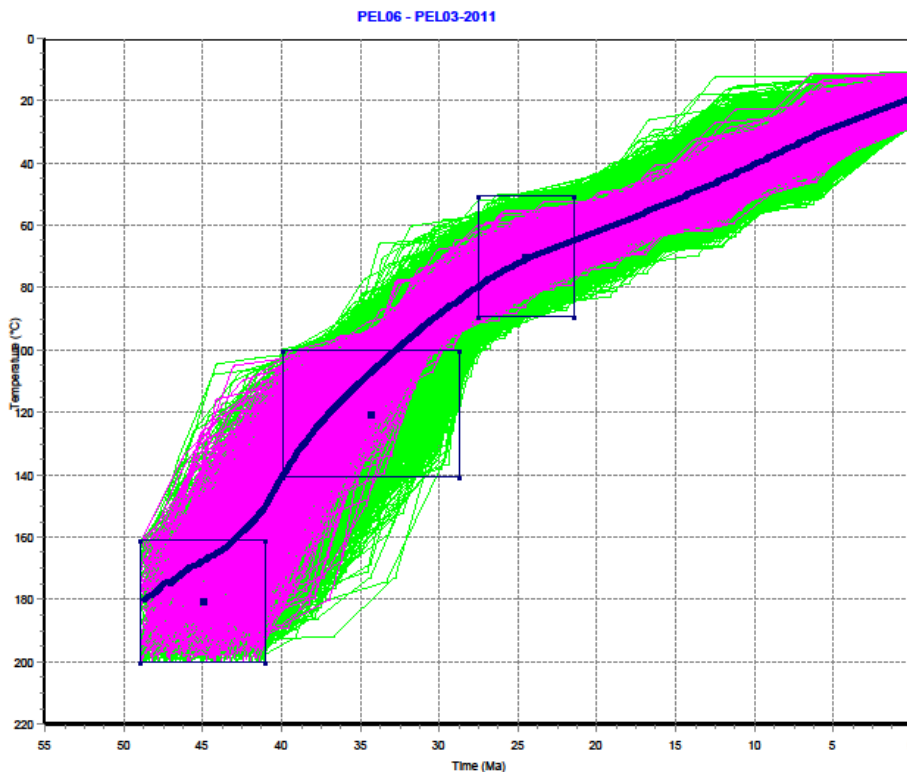
Figure 18. Thermal model for PEL06/PEL03-2011 from HeFTy software (Ketchum, 2005). Paths in green are acceptable fits, pink paths are good fits, black boxes are t-T constraint boxes.

56

The model for PEL04 was grouped with PEL02-2011, and generated 10000 paths, of which 235 were acceptable paths, and 31 were good paths (Table 5). The first constraint was 160°C-200°C / 55-51 Ma on PEL02-2011 ZHe data ran as a constraint box only. The second constraint was 100-140°C / 38-25 Ma on PEL04 AFT ran as a model. The third constraint was 50-90°C / 15-11 Ma on PEL02-2011-AP3 AHe data ran as a model. The final constraint was a present day temperature range of 15-20°C. The model for PEL04 / PEL02-2011, further northwest and closer to the tectonic windows, did generate a number of good paths which predict this pulse of rapid cooling between 15 and 7 Ma, and the weighted mean average suggests timing of this cooling event between 15-10 Ma.

The models for PEL06/PEL03-2011 and PEL04/PEL02-2011 suggest that crustal cooling has been ongoing here since at least ~50 Ma, and that the cooling rate (slope of the t-T curve) was elevated between 50-30 Ma but then slowed by 20 Ma. The weighted mean in the model for PEL06/PEL03-2011 suggests that this occurred gradually, however there is a large spread of good paths, some of which also suggest that this could have occurred rapidly. The model for PEL04/PEL02-2011 also has a large spread of good paths near the ZHe constraint, and does little to confirm whether the slowing of the cooling rate between 40-20 Ma occurred gradually or otherwise.
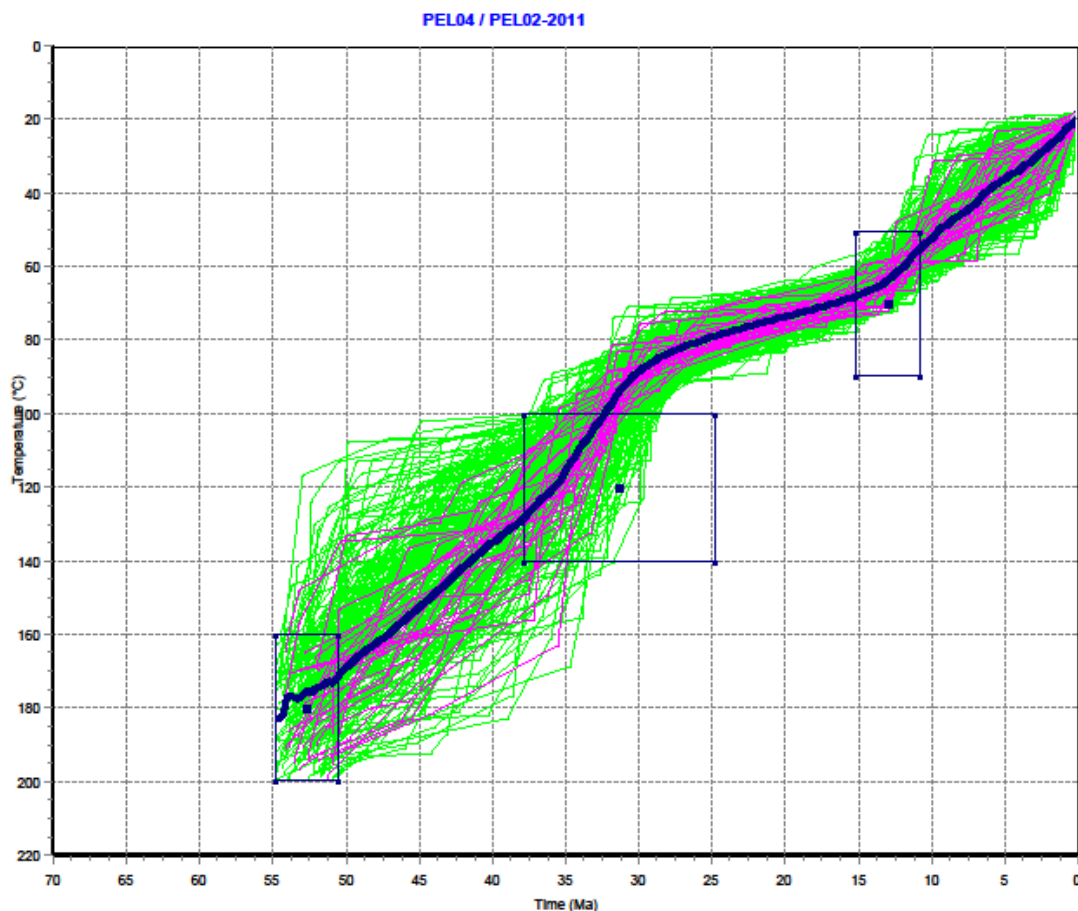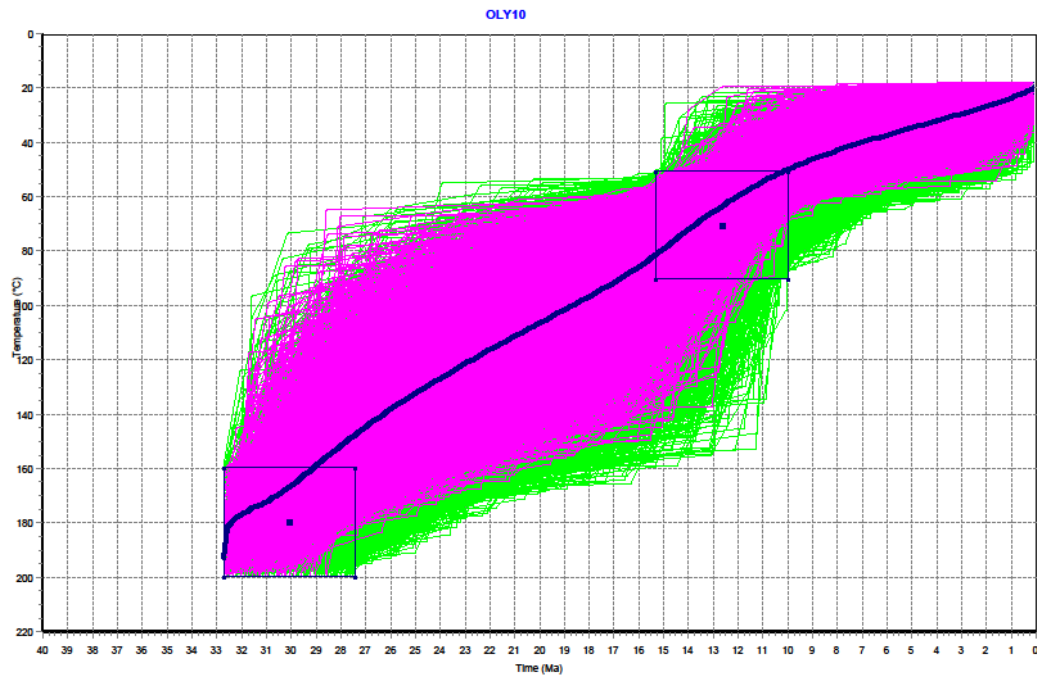
Figure 19. Thermal model for PEL04/PEL02-2011 from HeFTy software (Ketchum, 2005). Paths in green are acceptable fits, pink paths are good fits, black boxes are t-T constraint boxes.

The model for OLY10 generated 4746 acceptable paths and 3102 good paths(Table 5). The first constraint was 160-200°C / 32.5-27.5 Ma on OLY10-ZR1 ZHe data ran as a model. The second constraint was 50-90°/ 15.5-10 Ma on OLY10-AP4 AHe data ran as a model. The final constraint was a present day temperature range of 15-20°C. The model for OLY10, still in the Pelagonian zone, is lacking thermal data from AFT, and the model is effectively a weighted mean of all possible paths falling within diffusion and age parameters.

Figure 20. Thermal model for OLY10 from HeFTy software (Ketchum, 2005). Paths in green are acceptable fits, pink paths are good fits, black boxes are t-T constraint boxes.

The model for OLY09 generated 2790 acceptable paths and 685 good paths(Table 5). The first constraint was 160-200°C / 23-21 Ma on OLY09-ZR3 ZHe data ran as a model. The second constraint was 100-140°C / 18-12 Ma on OLY09 AFT data ran as a model. The third constraint was 50-90°C / 13.5-6.5 Ma on OLY09-AP6 AHe data ran as a model. The final constraint was a present day temperature range of 15-20°C. This model from OLY09, at the eastern most extent of the Pelagonian along the northernmost transect A-A' of figure 2 also does not tightly constrain the cooling path from ~11 Ma onward, but it does suggest that this rapid cooling event did not occur at this location prior to ~11 Ma.
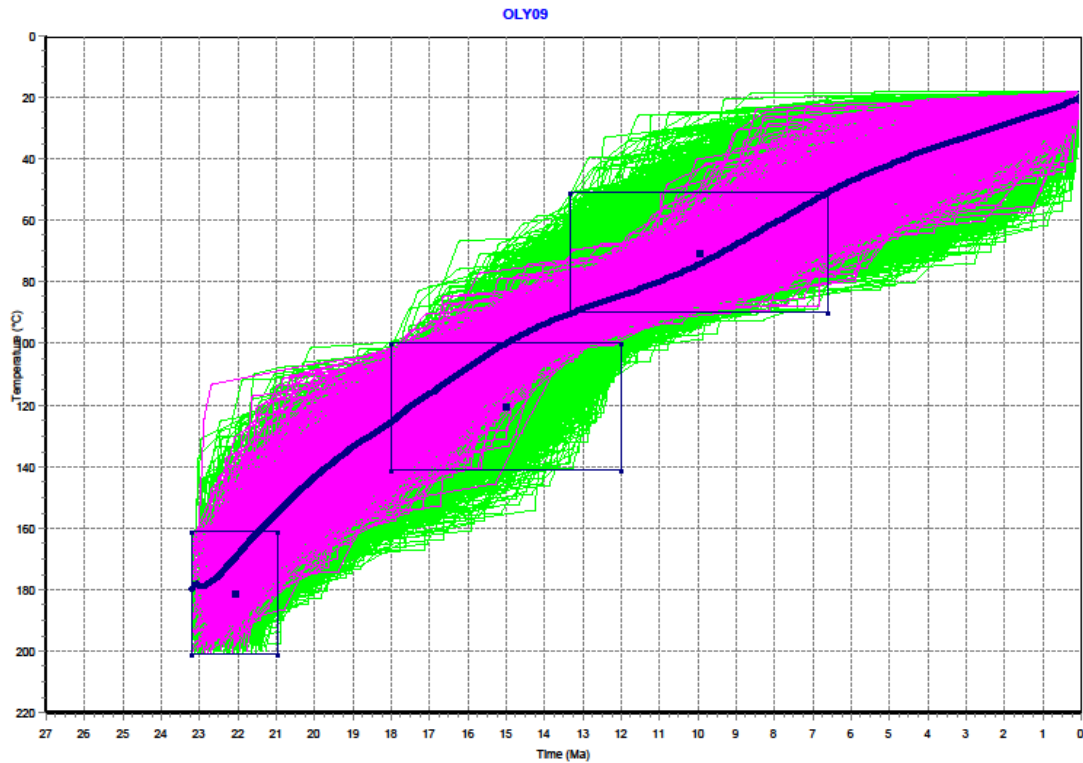
Figure 21. Thermal model for OLY09 from HeFTy software (Ketchum, 2005). Paths in green are acceptable fits, pink paths are good fits, black boxes are t-T constraint boxes.

The model for OLY06 generated 2790 acceptable paths and 1801 good paths (Table 5). The first constraint was 100-140°C / 14.7-10.3 Ma on OLY06 AFT data ran as a constraint box only as track length distributions was not available. The second constraint was 50-90°C / 11.7-9.7 Ma on OLY06-AP2 AHe data ran as a model. The final constraint was a present day temperature of 15-20°C. The model for OLY06, in the Ambelakia blueschists, constrain this cooling event with good paths showing this cooling event occurring between 14-11 Ma, with the weighted mean occurring between 14-13 Ma.
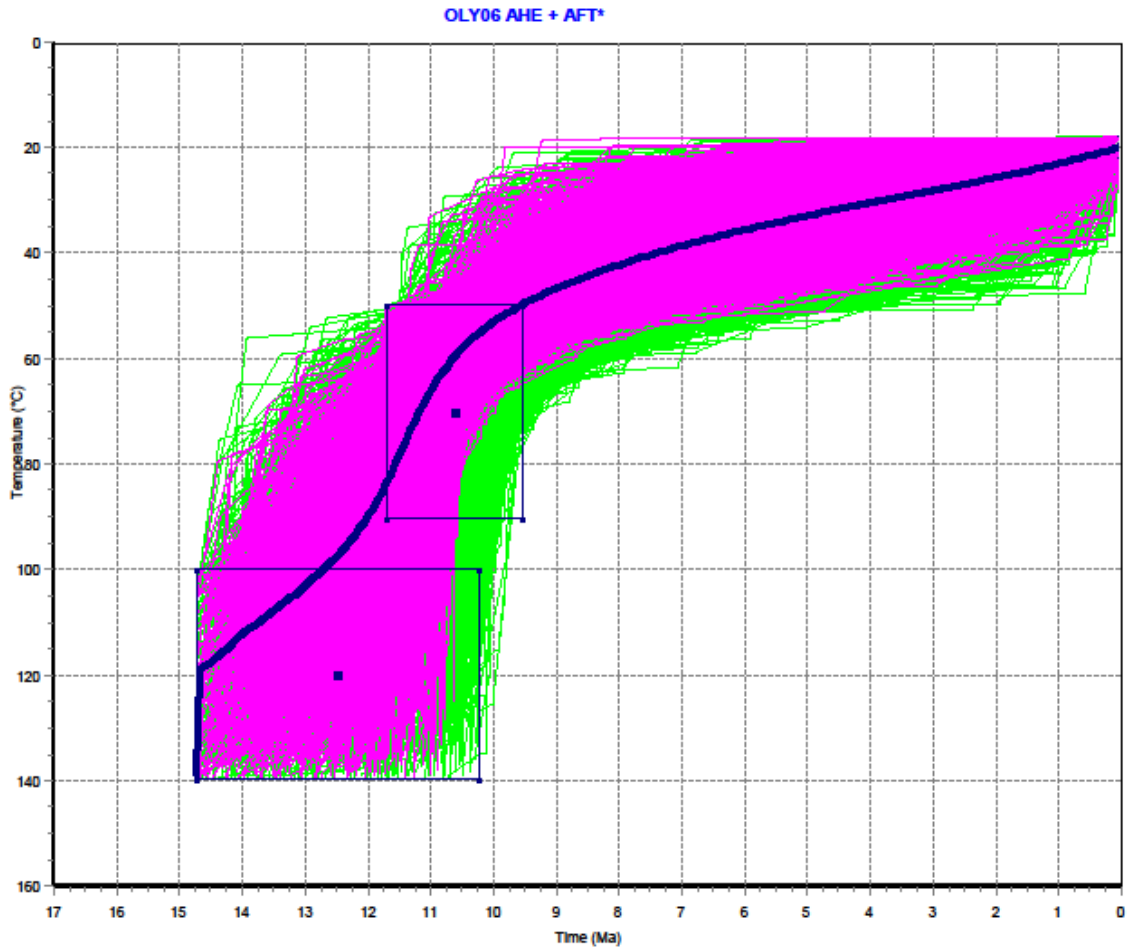
Figure 22. Thermal model for OLY06 from HeFTy software (Ketchum, 2005). Paths in green are acceptable fits, pink paths are good fits, black boxes are t-T constraint boxes.

In an attempt to improve upon the above Model for OLY06 and elucidate the cooling path at greater depths, it was also grouped with OLY07 and remodeled with OLY07-ZR3 ZHe data (Table 5). While OLY07 is not particularly close to OLY06 is close to the same contact between the Pelagonian zone and Ambelakia, and it also reports similar ZHe age as OLY01-2011 which lies to the northwest of OLY06. The model generated 1759 acceptable paths and 549 good paths. The additional constraint was 160-200°C / 24-22 Ma. Similar to the model for OLY06, this model constrains this cooling event with good paths showing this cooling event occurring between 14-11 Ma, with the weighted mean occurring between 14-13 Ma.
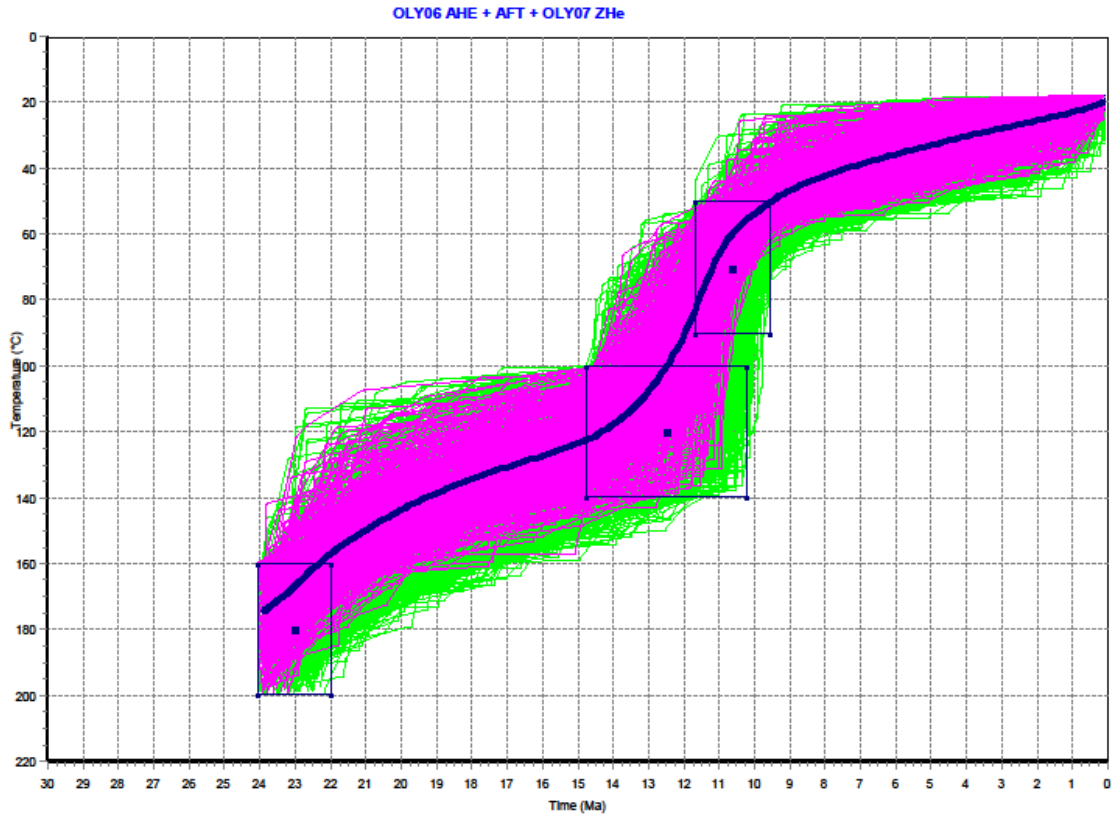
Figure 23. Thermal model for OLY06/OLY07 from HeFTy software (Ketchum, 2005). Paths in green are acceptable fits, pink paths are good fits, black boxes are t-T constraint boxes.

Table 5:
Summary of Thermal Modelling constraints and Results

Sample	PEL06 / PEL03-2011	PEL04 / PEL02-2011	OLY10	OLY09	OLY06	OLY06 / OLY07	OLY03 / OLY01-2011 / OLY06	OLY03 / OLY01-2011	OSSA04
First constraint	160-200°C	160-200°C	160-200°C	160-200°C	100-140°C	160-200°C	160-200°C	160-200°C	160-200°C
	49-41 Ma	55-51 Ma	32.5-27.5 Ma	23-21 Ma	14.7-10.3 Ma	24-22	24-22 Ma	24-22 Ma	14-10 Ma
Second constraint	100-140°C	100-140°C	50-90°C	100-140°C	50-90°C	100-140°C	100-140°C	100-140°C	100-140°C
	40-28 Ma	38-25 Ma	15.5-10 Ma	18-12 Ma	11.7-9.7 Ma	14.7-10.3 Ma	17-9.5 Ma	17-9 Ma	10.5-6.5 Ma
Third constraint (if applicable)	50-90°C	50-90°C		50-90°C		50-90°C	50-90°C		
	27.5-21.5 Ma	15-11 Ma		13.5-6.5 Ma		11.7-9.7 Ma	11.5-9.5 Ma		

62

Final constraint	15-20℃ Present	15-20℃ Present	15-20℃ Present	15-20℃ Present	15-20℃ Present	15-20℃ Present	15-20℃ Present	15-20℃ Present	15-20℃ Present
Paths	10000	10000	10000	10000	10000	10000	10000	10000	10000
Acceptable fits	3420	235	4746	2790	2790	1759	148	528	2828
Good fits	915	31	3102	685	1801	549	1	12	7172
Timing of Cenozoic Cooling	45.1-present	53.3-present	30.2-present	22.0-present	12.5-present	22.9-present	23.1-present	23.1-present	13.2-present
Average Cooling rate (℃/Ma) (to 20℃)	3.55	3.00	5.30	7.27	8.00	6.99	6.93	6.93	12.12
Temperature at 12.5 Ma (℃)	48	64	62	87	100	100	110	108	171
Average Cooling rate (℃/Ma) since 12.5 Ma	2.24	3.52	3.36	5.36	6.40	6.40	7.20	7.04	12.08

A grouped model for OLY06 with OLY03/OLY01-2011 generated 148 acceptable paths and 1 good path(Table 5). While OLY06 is ~4.3 km southwest of OLY03/OLY01-2011, it is still in the tectonic window of Olympus, and is the only nearby sample with AHe data. While this distance may bring the validity of this grouping into question, the general trend seen in the sample is in agreement with our other models. The first constraint was 160-200°C / 24-22 Ma on OLY01-2011-ZR5 ZHe data ran as a constraint box only. The second constraint was 100-140°C / 17-9.5 Ma on OLY03 AFT data ran as a model. The third constraint was 50-90°C / 11.5-9.5 Ma on OLY06-AP2 AHe data ran as a constraint box only. The final constraint was a present day temperature of 15-20°C. The model for OLY03/OLY01-2011/OLY06 show the cooling event occurring between 10-7 Ma.
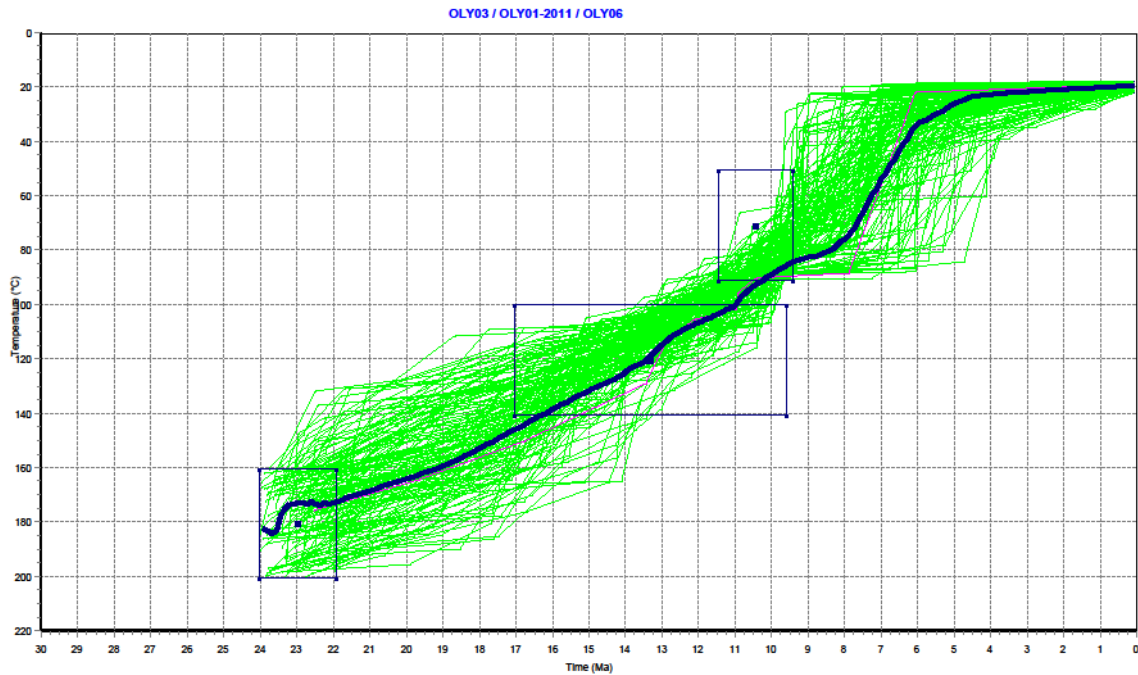
Figure 24. Thermal model for OLY03/OLY01-2011/OLY06 from HeFTy software (Ketchum, 2005). Paths in green are acceptable fits, pink paths are good fits, black boxes are t-T constraint boxes.

The model for OLY03 was grouped with OLY01-2011 (this time without OLY06) and generated 528 acceptable paths and 12 good paths(Table 5). The first constraint was 160-200°C / 24-22 Ma on OLY01-2011-ZR5 ZHe data ran as a constraint box only. The second constraint was 100-140°C / 17-9.5 Ma on OLY03 AFT data ran as a model. The final constraint was a present day temperature of 15-20°C. The model for OLY03/OLY01-2011 shows this cooling event occurring between 10-7 Ma.
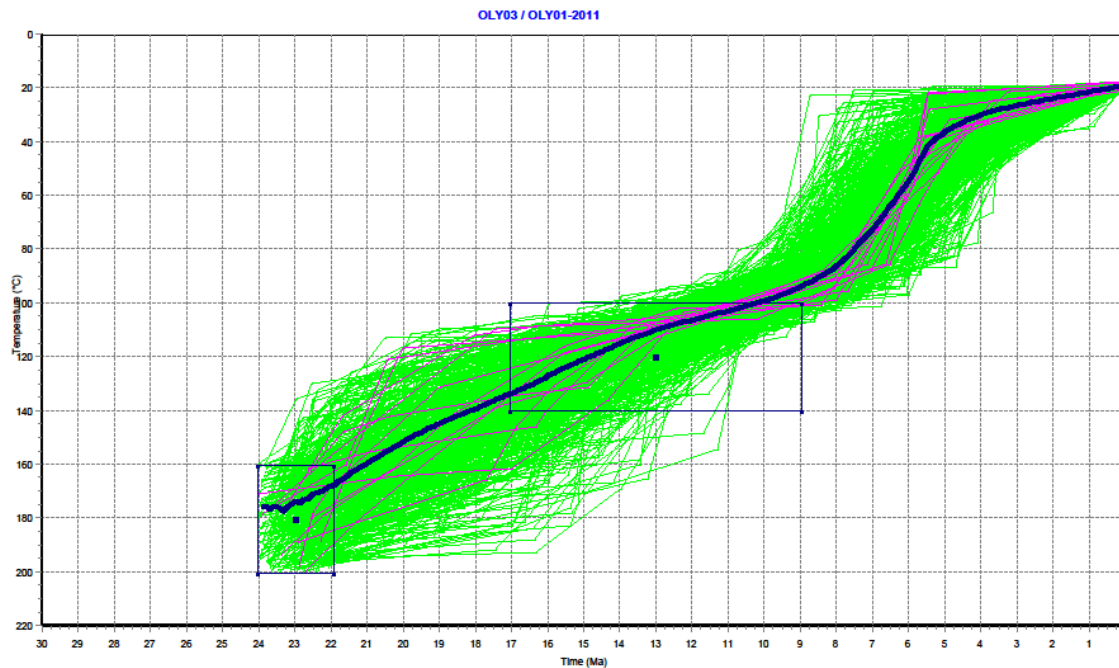
Figure 25. Thermal model for OLY03/OLY01-2011 from HeFTy software (Ketchum, 2005). Paths in green are acceptable fits, pink paths are good fits, black boxes are t-T constraint boxes.

The model for OSSA04 generated 2828 acceptable paths, and 7172 good paths (Table 5). first constraint was 160-200°C / 14-10 Ma on OSSA04-ZR4 ran as a model. The second constraint was 100-140°C / 10.5-6.5 Ma on OSSA04 AFT data ran as a constraint box only since track length distributions were not available for this sample. The final constraint was a present day temperature of 15-20°C. The model for OSSA04 shows a large spread of good paths, due to the absence of AFT track length data and AHe ages for the sample, and as such does little to constrain the cooling path.

For each model, and when possible, you should have provided cooling rates for the different segments of the cooling history.
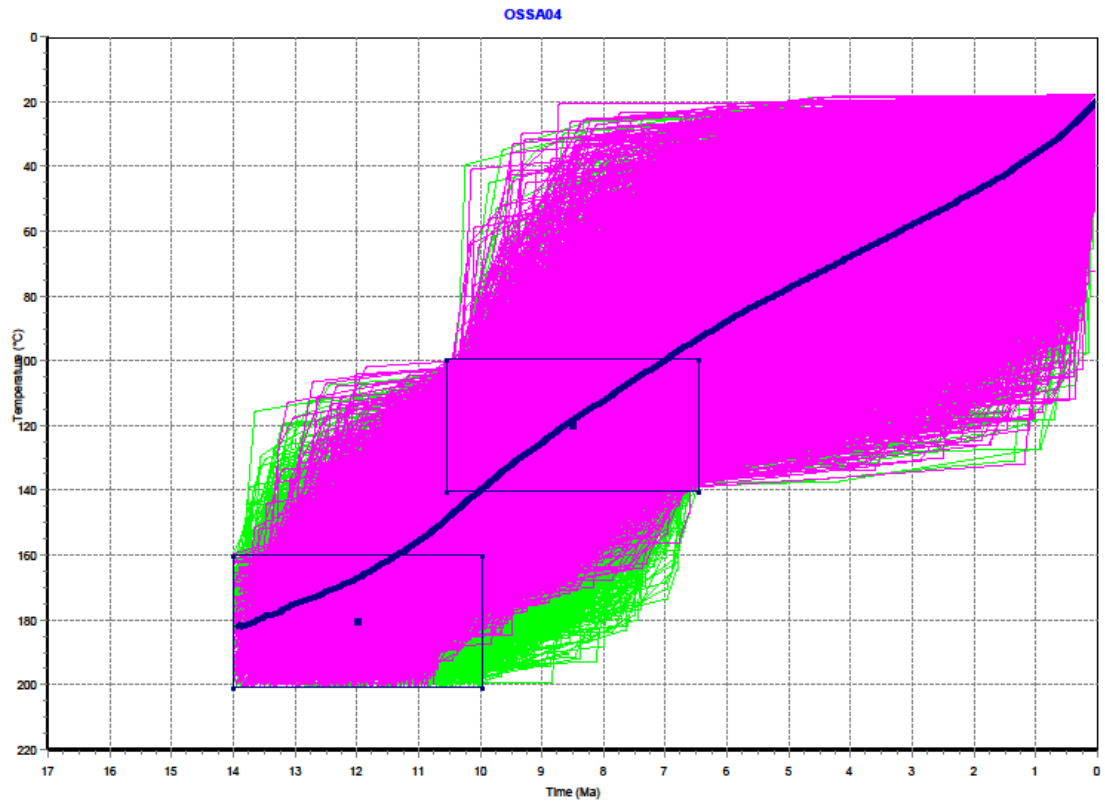
Figure 26. Thermal model for OSSA04 from HeFTy software (Ketchum, 2005). Paths in green are acceptable fits, pink paths are good fits, black boxes are t-T constraint boxes.

Chapter 5 - Discussion

5.1 - Crustal cooling trends throughout the study area

As suggested from the alpha corrected ages, the thermal models, and the calculated cooling rates, my interpretation of the data is that a rapid crustal cooling event occurred ~14-10 Ma ago and that this crustal cooling was more pronounced in the tectonic windows than in the Pelagonian Domain.

Cooling rates from 12.5 Ma until present were calculated and shown in Table 5. They show that cooling rates increase as samples progress towards the tectonic windows, with rates near Olympus that are > 3 times higher than Pelagonian samples in the southwest, and > 5 times higher near Ossa. Figure 28 shows a schematic of these rates along the transect A-A', and we can see that the lithologic contact of the Pelagonian/Ambelakia represents a sharp increase in crustal cooling rates, and that the rates continue to increase towards the Aegean fault, . This is in agreement with models of localized uplift in response to duplexing in the Olympus units, which would predict a sharp change in cooling rates. It may also represent localized isostatic rebound as a result of tectonic denudation. The data also indicate that the cooling rate is substantially higher within the Ossa massif than the Olympus massif. More thermochronological data could be collected along the Ambelakia blueschists, and Pindos outcroppings between OLY03 and OSSA04 to assess cooling relationships between Olympus and Ossa.
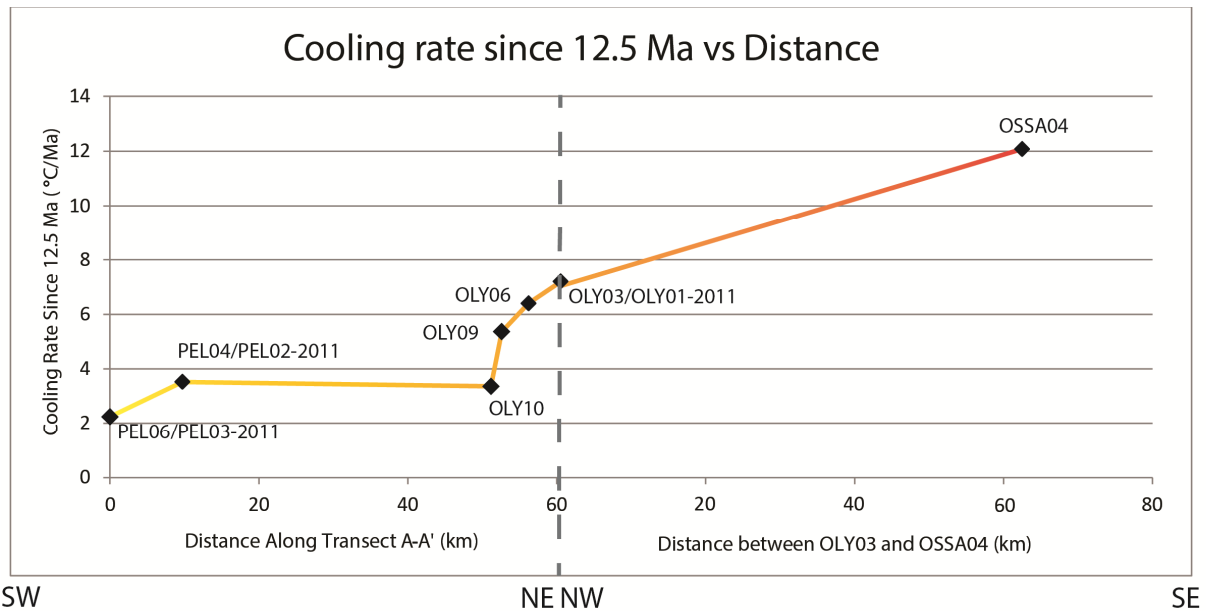
Figure 27: Cooling rate since 12.5 Ma versus distance in map view across transect A-A' (left side), and OLY03 to OSSA04 (Right side). Note the sharp increase in cooling rates beginning with sample OLY09, near the easternmost extent of the Pelagonian zone.

Hejl et al., (2010) constructed thermal models from the Kapidag Peninsula in the Sea of Marmara, and their results show similar elevated cooling rates from 45-30 Ma and slowing down thereafter. The timing of this elevated cooling rate is coeval with some of the older estimates for the onset subduction in the SHSZ as suggested from seismic tomography at around 40-26 Ma (Gautier et al., 1999).

5.2 - Rapid cooling event of the Olympus-Ossa massif

Taken these observations together, onset of this cooling event is estimated at 14-10 Ma across the tectonic windows and into the Pelagonian.

Following the rapid pulse of cooling, the models from the Pelagonian, and PEL04/PEL02-2011 in particular, provide little suggestion as whether the cooling rate remained constant until present, or spiked early and then slowed afterwards. Model OLY06/OLY07 from Ambelakia

shows that this rapid cooling event slows around 9-8 Ma and then cools slowly until present. This same trend is seen in Olympus model OLY03/OLY01-2001, where the rapid cooling event of the weighted average path slows between 5-4 Ma, with some acceptable fits occurring ~9 Ma and then cools slowly until present. So the data regarding this rapid cooling event suggest onset ~14-10 Ma, and lasting until ~9-5 Ma with slower cooling occurring thereafter. Previous Aegean thermochronological studies were conducted by Hejl et al, (2010) which obtained AFT ages in Mt Ossa, Pelion and Volos from 19.2 ± 3.2 Ma to 10.3 ± 0.7 Ma, in line with ages from this study. AFT thermochronology in the Sea of Marmara and the northern Aegean Sea suggest two cooling events. The first, between 35-25 Ma, and a second between 17-11.5 Ma (Hejl et al., 2010).

Another possibility to consider is that post-5 Ma cooling related to the NAF is not exposed in the modern landscape yet. This would create the possibility that another rapid cooling event occurred around 5 Ma, or that the cooling event initiated at 14-10 Ma continued through until some time post 5 Ma. For this to have occurred, the samples collected would have to have been at a sufficiently shallow depth at 5 Ma so that the proposed cooling event at 5 Ma did not cause the samples to be cooled through closure temperatures of the selected thermochronometers because they were already below those temperatures. This is similar to the discussion above as to why the 14-10 Ma cooling event was not seen clearly in the Pelagonian samples. If we look at the model for OLY06 / OLY07 (Fig. 23), this possibility can be eliminated. Due to the low temperatures of these samples at ~5 Ma, if another cooling event occurred ~5 Ma ago, these samples would have been exposed at surface ~4 Ma, and they would have long been eroded. A cooling event ~5 Ma would suggest crustal cooling of the samples stopped ~4 Ma, but since we know that the Aegean fault is currently still active, this possibility can be eliminated.

The data suggest that this cooling event predates NAF propagation into the Aegean domain by ages in excess of 5 Ma, and also postdates subduction zone initiation, estimated at 26-40 Ma.

69

There is also no known evidence that there was any increased rate of subduction zone migration occurring at this time which could have led to increased footwall cooling. The data point to the conclusion that the propagation of the NAF itself at 5 Ma into the Aegean domain did not cause a crustal cooling event, but rather it was caused by events occurring beforehand.

Hejl et al., (2010) obtained thermal histories from AFT data from the island of Samothrake, in the shoulder of an active pull-apart basin along the NAF in the northern Aegean domain (Fig. 28). The results were interpreted as rapid cooling from transtension between 14-10 Ma (Hejl et al., 2010). These ages, combined with structural observations from the Ganos fault (Section 2.13) (Yaltirak and Alpar, 2002), and thermal models from this study suggest that discontinuous faulting, and transtensional structures were in fact active in the Aegean before NAF propagation reached the area (Hejl et al., 2010).
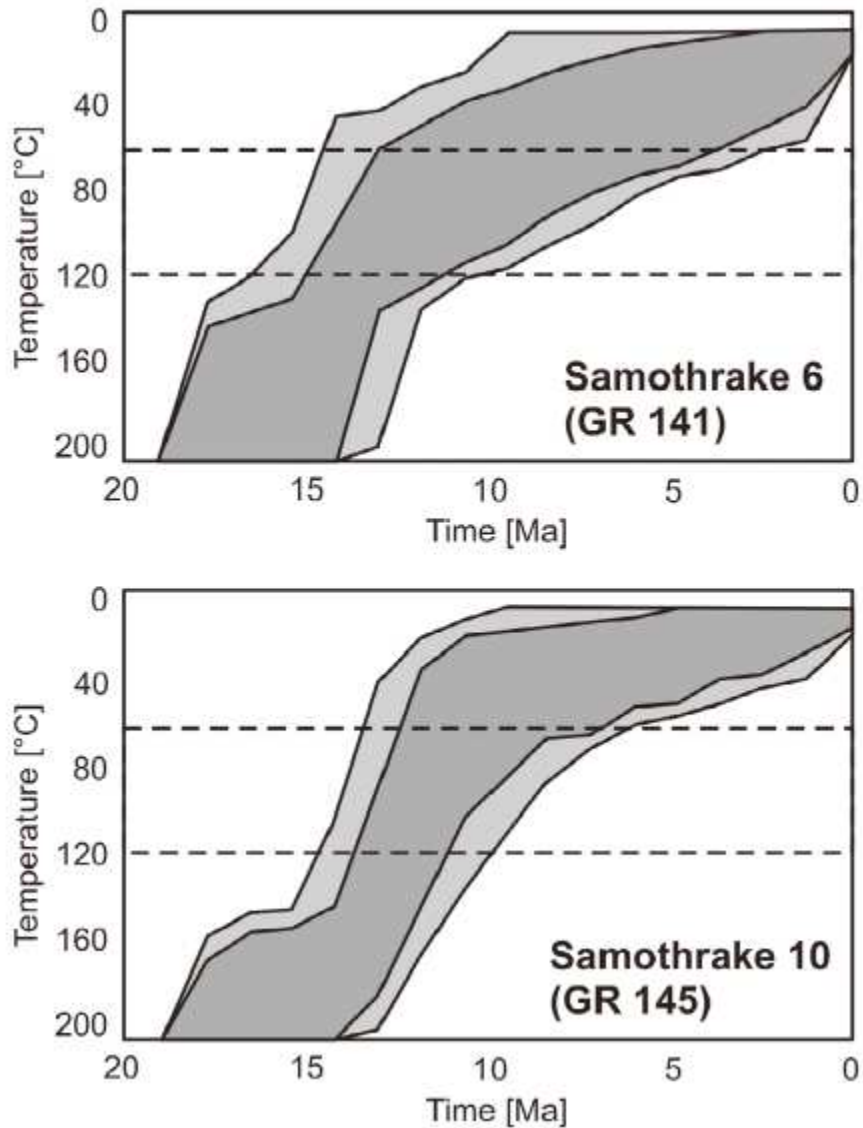
Figure 28: Thermal histories from the Island of Samothrake in the Aegean Sea, interpreted as indicating a rapid cooling event between 14-10 Ma (From Hejl et al., 2010)

It is my interpretation that displacement along these early precursors to the North Anatolian Fault, similar to ones documented above, facilitated displacement along the normal Aegean fault and led to the rapid cooling event seen in the Olympus and Ossa massifs between 14-10 Ma.

Chapter 6 - Conclusion

(U-Th)/He dating combined with apatite fission-track in the region around Mount Olympus has revealed a rapid cooling event at 14-10 Ma. This event reflects a period prior to NAF propagation in which discontinuous faults, which have been noted in the Aegean and were later incorporated into the North Anatolian Fault, facilitated rapid cooling in the footwall of the Aegean fault. The timing of this rapid cooling event in the Olympus and Ossa massifs can be correlated with a similar cooling event throughout the northern Aegean (Hejl et al., 2010) and is not coeval with the onset of subduction in the SHSZ which has been estimated between 40-26 Ma.

References

Armijo, R., B. Meyer, A. Hubert, and A. Barka (1999), Westward propagation of the North Anatolian Fault into the northern Aegean: Timing and kinematics. Geology, 27: 267–270.

Bargnesi, E.A., Stockli, D.F., Mancktelow, N., Soukis, K. (2012) Miocene core complex development and coeval supradetachment basin evolution of Paros, Greece, insights from (U–Th)/He thermochronometry. Tectonophysics. Available online 28 July 2012, ISSN 0040-1951

Berckhemer, H., (1977) Some aspects of the evolution of marginal seas deduced from observations in the Aegean region. In: Biju-Duval, B., Montadert, L. (Eds.), Int. Symp. Struc tural History of the Mediterranean Basins, Split, Yugosla via, 25–29 October 1976. Technip, Paris, 303–313.

Ehlers, T.A. (2005) Crustal Thermal Processes and the Interpretation of Thermochronometer Data, Reviews in Mineralogy and Geochemistry. 58: 315-350

England, P., Molnar, P., (1990) Surface uplift, uplift of rocks, and exhumation of rocks. Geology. 18: 1173-1177

Farley, K.A., (2002) (U-Th)/He Dating: Techniques, Calibrations, and Applications. Reviews in Mineralogy and Geochemistry. 47: 819-844

Ferriere, J., Reynaud, J., Pavlopoulos, A., Bonneau, M., Migiros, G., Chanier, F., Proust, J., Gardin, S. (2004) Geologic evolution and geodynamic controls of the Tertiary intramontane piggyback Meso-Hellenic basin, Greece. Bull. Soc. Geol. Fr. 175: 361-381

Flerit, F., Armijo, R., King, G., Meyer, B., The mechanical interaction between the propagating North Anatolian Fault and the back-arc extension in the Aegean. Earth and Planetary Science Letters. 224: 347-362

Gautier P., Brun J.P., Moriceau R., Sokoutis D., Martinod J., Jolivet L., (1999) Timing, kinematics and cause of Aegean extension: a scenario based on a comparison with simple analogue experiments. Tectonophysics 315: 31–72.

Hejl, E., J. De Grave, H. Riedl, H. Weingartner, and P. Van den haute (2008), Fission track thermochronology of the Middle Aegean Island Bridge — Implications for Neogene geomorphology and palaeogeography, Zeitschrift der deutschen Gesellschaft für Geowissenschaften, 159/3: 495–512.

Hejl, E., Bernroider, M., Parlak, O., Weingartner, H. (2010) - Fission-track thermochronology, vertical kinematics, and tectonic development along the western extension of the North Anatolian Fault zone. Journal of Geophysical Research. 115: 148-227

Ketcham, R.A., (2005) Forward and Inverse Modeling of Low-Temperature Thermochronometry Data. Reviews in Mineralogy and Geochemistry 58: 275-314

Ketcham, R.A., (2005) Forward and Inverse Modeling of Low-Temperature Thermochronometry Data. Reviews in Mineralogy and Geochemistry. 58: 275-314

Ketcham, R.A., (2011) Accounting for long alpha-particle stopping distances in (U–Th–Sm)/He geochronology: Refinement of the baseline case. Geochemica et Cosmochemica Acta. 75: 7779-7791

Ketcham, R.A., (2013) HeFTy Version 1.8.0. Apatite to Zircon, Inc. and Richard A Ketcham.

Kilias, A., Tranos, M.D., Orozco, M., AlonsoChaves, F.M. and Soto, J.I., (2002) Extensional collapse of the Hellenides: A review. Revista de la Sociedad Geologice de Espana. 15:129-139.

Jolivet, L., Brun, J.P., (2010) Cenozoic geodynamic evolution of the Aegean. Int Journal Earth Science. 99:109-138

Lacassin, R., Arnaud, N., Leloup, P.H., Armijo, R., Meyer, B., (2007) Syn- and post-orogenic exhumation of metamorphic rocks in North Aegean. eEarth Discuss. 2: 51-63

Meesters, A.G., Dunai, T.J. (2005) A noniteritive solution of the (U-Th)/He age equation. Geochemistry, Geophysics, Geosystems. 6/4: 1525-1527

Nance, D., (2010) Neogene–Recent extension on the eastern flank of Mount Olympus, Greece. Tectonophysics. 488: 282-292

Reiners, P.W., (2005) Zircon (U-Th)/He Thermochronometry. Reviews in Mineralogy and Geochemistry. 58: 151-179

Reiners, P.W., Brandon, M.T. (2006) Using Thermochronology to Understand Orogenic Erosion. Annual Rev. Earth Planet Sci. 34: 419-466

Reiners, P.W., Ehlers, T.A., Zeitler, P.K. (2005) Past Present, and Future of Thermochronology, Reviews in Mineralogy and Geochemistry. 58: 1-18

Ryan,W. B. F., Cita, M. B., (1978) The nature and distribution of Messinian erosional surfaces—Indicators of a several-kilometer-deep Mediterranean in the Miocene. Marine Geology, 27:193–230

Schermer, E.R., Lux, D.R., Burchfiel B.C., (1990) Temperature-time history of subducted continental crust, Mount Olympos region, Greece. Tectonics 9:1165–1195.

Schermer, E.R., (1993) Geometry and kinematics of continental basement deformation during the Alpine orogeny, Mt. Olympos region, Greece. J Struct Geol 15:571–591.

Stockli, D.F. (2005) Application of Low-Temperature Thermochronometry to Extensional Tectonic Settings. Reviews in Mineralogy and Geochemistry. 58: 411-448

Thompson, S.N., Stockhert, B., Brix, M.R., (1998) Thermochronology of the high-pressure metamorphic rocks of Crete, Greece: Implications for the speed of tectonic processes. Geology. 26/3: 259-262

Yaltirak, C., and B. Alpar (2002), Kinematics and evolution of the northern branch of the North Anatolian Fault (Ganos Fault) between Sea of Marmara and the Gulf of Saros, Mar. Geol., 190: 351–366.